NASA-CR-191393

MARSHALL GRANT

IN-90-CR

135392

P-51

FINAL REPORT
FROM
THE MASSACHUSETTS INSTITUTE OF TECHNOLOGY
TO
THE NATIONAL AERONAUTICS AND SPACE ADMINISTRATION
ON
NASA GRANT NAG8-701

THE ATMOSPHERIC STRUCTURES OF THE COMPANION STARS OF ECLIPSING BINARY X-RAY SOURCES

Principal Investigator: Professor George W. Clark
MIT 37-611
Cambridge, MA 02139
Tel: (617) 253-5842

ORIGINAL PAGE IS
OF POOR QUALITY

(NASA-CR-191393) THE ATMOSPHERIC STRUCTURES OF THE COMPANION STARS OF ECLIPSING BINARY X RAY SOURCES Final Report (MIT) 51 p

N93-16752

Unclas

G3/90 0135392

INTRODUCTION

This investigation was aimed at determining structural features of the atmospheres of the massive early-type companion stars of eclipse X-ray pulsars by measurement of the attenuation of the X-ray spectrum during eclipse transitions and in deep eclipse. Several extended visits were made to ISAS in Japan by G. Clark and his graduate student, Jonathan Woo to coordinate the Ginga observations and preliminary data reduction, and to work with the Japanese host scientist, Fumiaki Nagase, in the interpretation of the data.

At MIT extensive developments were made in software systems for data interpretation. In particular, a Monte Carlo code was developed for a 3-D simulation of the propagation of X-rays from the neutron star through the ionized atmosphere of the companion. With this code it was possible to determine the spectrum of Compton-scattered X-rays in deep eclipse and to subtract that component from the observed spectrum, thereby isolating the soft component that is attributable in large measure to X-rays that have been scattered by interstellar grains.

This research has culminated in the submission of a paper to the Astrophysical Journal on the determination of properties of the atmosphere of QV Nor, the B0 I companion of 4U 1538-52, and the properties of interstellar dust grains along the line of sight from the source. The latter results were an unanticipated byproduct of the investigation.

Data from Ginga observations of the Magellanic binaries SMC X-1 and LMC X-4 are currently under investigation as the PhD thesis project of Jonathan Woo who anticipates completion in the spring of 1993.

SUMMARY OF RESULTS

From measurements of the X-ray eclipse phenomena of the binary X-ray pulsar 4U 1538-52 we have derived properties of the stellar wind of its B0 I companion, QV Nor, and evidence of the fluffy nature of interstellar grains. The average density of atoms at a distance r from the center of QV Nor, deduced from analysis of the variation of X-ray attenuation during an eclipse egress, is described by an exponential function with a scale height of 4.5×10^{10} cm joined smoothly at $r=1.22r_0$ to a function of the form $\dot{M}/(4\pi r^2 \mu v_t)$, where $\dot{M}/v_t=1.19\times10^{-9}\ M_\odot\ \mathrm{yr}^{-1}\ \mathrm{km}^{-1}$ s is the ratio of the mass loss rate to the terminal velocity, $r_0=0.97\times10^{12}$ cm is the nominal stellar radius, and μ is the mean atomic mass. A Monte Carlo computation of the absorption and scattering of X-rays in the X-ray-ionized circumstellar matter accounts well for the spectrum of X-rays with energies above 4.5 keV observed during the eclipse, while below 4.5 keV there is a component of soft X-rays above the Monte Carlo prediction with a total photon flux amounting to approximately 1.4% of the uneclipsed flux in the same energy range. A portion of the soft component may be thermal emission from shock-heated plasma in the flow disturbances caused by passage of the neutron star through the stellar wind. The remaining portion is attributed to grain-scattered X-rays that are delayed in arrival relative to X-rays that come directly from the neutron star. To facilitate a comparison of the X-ray scattering and optical extinction caused by interstellar grains

we introduce a quantity $R_{XV}(E)$, which we define as the ratio of the fractional intensity of grain-scattered X-rays of energy E to the optical extinction at wavelength 5550 Å. Taking the total intensity of the soft component as an upper limit on the grain-scattered intensity, and the lower bound on the optical extinction of QV Nor as $A_V \geq 6.4$ mag, we set an upper bound on $R_{XV}(E=2\text{ keV})$ of 0.0047 ± 0.0004 which is much less than the predicted value of R_{XV} for compact spherical dielectric grains with a density ~3 g cm^{-3} and a size distribution that extends to radii greater then 0.1 μm. The upper bound on R_{XV} is, however, compatible with a simplistic model of interstellar grains as "fluffy" spherical aggregates consisting of 80% of vacuum and 20% of particles composed of material with a refractive index like that of "dirty ice" and a mean specific density of 1.2, together with a distribution in radius of the grains in the form of the power law $n_g(a) \sim a^{-3.7}$ with $0.001 \mu\text{m} < a < 0.3\ \mu\text{m}$.

PUBLICATION

Attached to this Final Report is a copy of the paper submitted for publication in the Astrophysical Journal.

PROPERTIES OF A B0 I STELLAR WIND AND INTERSTELLAR GRAINS DERIVED FROM *GINGA* OBSERVATIONS OF THE BINARY X-RAY PULSAR 4U 1538-52

George W. Clark and Jonathan W. Woo
Center for Space Research and Department of Physics
Massachusetts Institute of Technology, Cambridge, MA 02139
and
Fumiaki Nagase
The Institute of Space and Astronautical Science
3-1-1, Yoshinodai, Sagamihara, Kanagawa 229, Japan

ABSTRACT

From measurements of the X-ray eclipse phenomena of the binary X-ray pulsar 4U 1538-52 we have derived properties of the stellar wind of its B0 I companion, QV Nor, and evidence of the fluffy nature of interstellar grains. The average density of atoms at a distance r from the center of QV Nor, deduced from analysis of the variation of X-ray attenuation during an eclipse egress, is described by an exponential function with a scale height of 4.5×10^{10} cm joined smoothly at $r = 1.22 r_0$ to a function of the form $\dot{M}/(4\pi r^2 \mu v_t)$, where $\dot{M}/v_t = 1.19 \times 10^{-9}\ M_\odot\ \mathrm{yr}^{-1}\ \mathrm{km}^{-1}$ s is the ratio of the mass loss rate to the terminal velocity, $r_0 = 0.97 \times 10^{12}$ cm is the nominal stellar radius, and μ is the mean atomic mass. A Monte Carlo computation of the absorption and scattering of X-rays in the X-ray-ionized circumstellar matter accounts well for the spectrum of X-rays with energies above 4.5 keV observed during the eclipse, while below 4.5 keV there is a component of soft X-rays above the Monte Carlo prediction with a total photon flux amounting to approximately 1.4% of the uneclipsed flux in the same energy range. A portion of the soft component may be thermal emission from shock-heated plasma in the flow disturbances caused by passage of the neutron star through the stellar wind. The remaining portion is attributed to grain-scattered X-rays that are delayed in arrival relative to X-rays that come directly from the neutron star. To facilitate a comparison of the X-ray scattering and optical extinction caused by interstellar grains we introduce a quantity $R_{XV}(E)$, which we define as the ratio of the fractional intensity of grain-scattered X-rays of energy E to the optical extinction at wavelength 5550 Å. Taking the total intensity of the soft component as an upper limit on the grain-scattered intensity, and the lower bound on the optical extinction of QV Nor as $A_V \geq 6.4$ mag, we set an upper bound on $R_{XV}(E = 2\ \mathrm{keV})$ of 0.0047 ± 0.0004 which is much less than the predicted value of R_{XV} for compact spherical dielectric grains with a density $\sim 3\ \mathrm{g\ cm^{-3}}$ and a size distribution that extends to radii greater then 0.1 μm. The upper bound on R_{XV} is, however, compatible with a simplistic model of interstellar grains as "fluffy" spherical aggregates consisting of 80% of vacuum and 20% of particles composed of material with a refractive index like that of "dirty ice" and a mean specific density of 1.2, together with a distribution in radius of the grains in the form of the power law $n_g(a) \sim a^{-3.7}$ with $0.001\,\mu\mathrm{m} < a < 0.3\ \mu\mathrm{m}$.

Subject Headings: Binaries: Eclipsing – Interstellar: Grains – Stars: Winds – X-Rays: Binaries – Pulsars: Individual (4U 1538-52)

1. INTRODUCTION

The eclipse phenomena of massive X-ray binaries are sources of unique information about the atmospheric structures of their primaries. The latter are generally massive O or B0 stars with intense radiatively-driven supersonic winds. Measurements of X-ray eclipse transitions probe the density structures of these winds over the range of radius in which the flow crosses the sonic point. In several of the massive X-ray binaries whose eclipse transitions have been analyzed in detail (Clark, Minato & Mi 1988; Day & Stevens 1992; Lewis et al. 1992) the average runs of density in this range are found to conform to exponential functions of radius with scale heights of the order of a 1/20 of the stellar radii, in disagreement with the density functions derived in steady-state theories of radiatively driven winds based on the Sobolev approximation. X-ray eclipse transition measurements therefore provide clues for the development of more realistic theories that avoid the Sobolev approximation and take account of instabilities in the radiation-driving mechanism.

The X-rays observed in eclipse cast light on several aspects of the circumsource and interstellar environment. Circumsource material scatters X-rays into the umbra with a spectrum similar to that of the average uneclipsed spectrum and an intensity that is a measure of $\dot{M}/v_t$, the ratio of the mass-loss rate to the terminal velocity of the wind. X-ray-excited fluorescence and thermal emission from the same matter, excited by the pulsar X-rays and by shock-heating, contribute a soft continuum and emission lines. Scattering from interstellar grains produces a halo around the point-like source that persists during an eclipse due to transit time delays. And finally, the primary star itself is a source of coronal X-rays, though generally of such relatively low intensity as to be negligible in comparison with the direct or induced effects of the pulsar radiation.

Our purpose in this investigation was to derive from the X-ray eclipse phenomena of 4U 1538-52 properties of the stellar wind of its heavily reddened B0 I companion, QV Nor. We sought a model of the pulsar X-ray emission spectrum and the distribution of X-ray ionized circumsource matter that yields a comprehensive explanation of the observed X-ray and optical phenomena of the system. In addition we derived a constraint on the composition and size distribution of interstellar grains from an analysis of the X-ray spectrum in eclipse and the optical extinction of QV Nor.

Lucy and Solomon (1970) suggested that radiation pressure due to scattering of stellar ultraviolet radiation in Doppler-shifted resonance absorption lines drives the cool ($T \sim 10^{4.6}$ K) winds of early-type stars to supersonic velocities with mass-loss rates of the order of $10^{-6}\ M_{\odot}\ \mathrm{yr}^{-1}$. Steady-state theories based on this idea stem in large part from the work of Castor, Abbott, & Klein (1975) who developed a model that takes account of the multiplicity of UV resonance lines and conforms to the condition of a smooth transition from subsonic to supersonic flow. Their theory and later refinements (e.g., Abbott 1980, 1982; Friend & Abbott 1986) employed the Sobolev approximation in which it is assumed that the density and other parameters that characterize the flow are approximately constant over distances in which the flow velocity increases by an ion thermal speed (Cassinelli 1979, and references therein). Steady-state theories predict velocity functions in the supersonic regimes of early-star winds and mass-loss rates that are in general agreement with observations of ultraviolet P Cygni line profiles. Velocity curves derived in these theories have often been approximated by a power law of the form

$$v = v_0 + (v_t - v_0)(1 - r_0/r)^\beta , \quad r > r_0, \tag{1.1}$$

where r_0 and v_0 are the radius and velocity of the wind at the stellar "surface", v_t is the terminal velocity, and β in the range from 0.5 to 1.5. With β=0.5 and v_0=0 this function represents the velocity of an isolated particle starting from rest at r_0 and driven outward by a force diminishing as the square of the distance. Used in the interpretation of data that pertain to the supersonic regime, such as UV P Cygni profiles and radio and infrared measurements, it implies a rapid initial acceleration and a corresponding rapid initial decline in the density.

The Sobolev approximation is, however, grossly inaccurate in the subsonic regime. Moreover, the steady-state assumption is belied by the ubiquitous coronal X-ray emission of early-type stars (Cassinelli et al. 1981) which has been attributed to localized heating by shocks that arise from instabilities inherent in the radiation-driving mechanism (Lucy & White 1980). Non-steady flow in the supersonic region is also revealed directly by the observation of variable discrete narrow absorption features within P Cygni profiles (Prinja & Howarth 1986). This evidence of non-steady flow implies that the density function which one can infer from a column density profile measured during an X-ray eclipse transition is a path average over a spectrum of density fluctuations.

To demonstrate the relevance of eclipsing X-ray binaries to the investigation of the structure of stellar winds we estimate the wind velocity in the region probed by analysis of X-ray attenuation during an eclipse transition. The column particle density N_H of hydrogen atoms along a line of sight that passes the primary at a distance r where the particle density is n can be estimated as $N_H \approx nr$. If the wind velocity at this radius is v, then the mass-loss rate is $\dot{M} = 4\pi r^2 \mu n v$, where $\mu = 1.34 m_H$ is the average atomic mass per hydrogen atom. Solving for the velocity, we find

$$v \approx 23\ \dot{M}\ (10^{-6} M_\odot \mathrm{yr}^{-1})\ N_H (10^{24} \mathrm{cm}^{-2})^{-1} r (10^{12} \mathrm{cm})^{-1}\ \mathrm{km\ s}^{-1} . \tag{1.2}$$

The column density for 1/e attenuation of an X-ray beam in cold matter with normal cosmic abundances ranges from $\sim 10^{23}$ to $\sim 10^{24}$ H-atoms cm^{-2} in the energy range from 3.5 to 15 keV. The isothermal velocity of sound at 4×10^4 K is ~20 km s^{-1}. Thus, measurements of the changes in the X-ray spectrum in the energy range from 3.5 to 15 keV during an eclipse transition probe the density profile of the wind in the region of transition from subsonic to supersonic flow where the singularity in the hydrodynamic equation for steady flow occurs.

The fractional intensity of X-rays in eclipse due to Compton scattering by matter in a wind that moves with nearly its terminal velocity in the region beyond the orbit of the pulsar can be estimated as

$$\frac{\sigma_{\mathrm{T}}\dot{\mathrm{M}}}{2\pi\mu v_{\mathrm{t}} s} \approx 0.015\ \dot{\mathrm{M}}\ (10^{-6}\mathrm{M}_{\odot}\mathrm{yr}^{-1})\ v_{\mathrm{t}}\ (2\mathrm{x}10^{3}\ \mathrm{km\ s}^{-1})^{-1}\ s\ (10^{12}\ \mathrm{cm})^{-1}, \qquad (1.3)$$

where σ_{T} is the Thomson cross section, and s is the distance between the star centers. Thus, with a stellar wind typical of B0 supergiants like the companion of 4U 1538-52, one can expect the Compton-scattered component of the X-ray intensity in eclipse to have a spectrum similar to the average uneclipsed spectrum with an intensity proportional to $\dot{\mathrm{M}}/v_{\mathrm{t}}$ and ~1-2 % of the uneclipsed intensity.

Finally, we point out that an eclipsing X-ray binary offers a unique advantage for the study of interstellar grains. The angular distribution of X-rays in the image of an X-ray source consists of a "core" component that comes directly from the star or its immediate vicinity, and a generally much fainter "halo" component that has been scattered by interstellar grains near the line of sight, as predicted by Overbeck (1965) and discussed by him and others (Hayakawa 1970; Martin 1970) before the availability in orbit of imaging X-ray telescopes. Measures of the intensities of Overbeck halos have since been derived from analyses of X-ray star images in which the halo is dissected from the much brighter core by subtraction of the point-spread function of the telescope (e.g., Mauche & Gorenstein 1986, hereafter MG; Predehl et al. 1991). In addition, the halo intensity of a source near the galactic center has been measured with a non-imaging detector during a brief time following a lunar occultation of the core component (Mitsuda et al. 1990). In an eclipsing binary at a distance of several kpc, the halo will persist long after the neutron star is eclipsed by its primary because the average travel time of the grain scattered X-rays is many hours longer than the travel time of the undeviated X-rays in the core. Since the X-ray scattering efficiency of small particles varies as E^{-2}, the spectrum of the grain-scattered X-rays is much softer than the uneclipsed core spectrum. Consequently, when the core intensity is reduced by the eclipse, the grain-scattered intensity may stand out as a distinct "soft component" that gradually decays with time after ingress. Since the optical extinction and the fractional intensity of grain-scattered X-rays depend on the size, composition and density of the grains in quite different ways, a determination of the quantitative relation between these two observables can be used to place a critical constraint on models of interstellar grains. Analysis of high-resolution X-ray images of binary X-ray stars in eclipse will clearly be the best way to exploit such opportunities in the future. Nevertheless, we have obtained significant results from an analysis of the non-imaging data from *Ginga*.

The first observations of a column density profile during an X-ray eclipse transition in a massive X-ray binary were reported from *Uhuru* observations of Cen X-3 by Schreier et al. (1972) who found an exponential scale height of $h \approx 5\mathrm{x}10^{10}$ cm for the atmosphere of its companion. In addition they found residual intensity in eclipse on the order of 1% of the uneclipsed intensity. More extensive studies of the eclipse transitions of Cen X-3 and their implications for the structure of the stellar wind of the primary were made with SAS-3 (Clark et al. 1988) and *Exosat* (Day & Stevens 1992), with similar results concerning the exponential form of the lower atmospheric density and the magnitude of its scale height. X-ray eclipse transitions have been studied in Vela X-1 by Sato et al. (1986) and Lewis et al. (1992), and in 4U 1538-52 by Makishima et al. (1987), with results that are fitted by exponential density functions in the lower atmospheres of the companion stars with scale heights of the order of a tenth of the stellar radii. On the other hand, Haberl, White, & Kallman (1989) found that the column density profile of the wind in the O6.5f companion of 4U 1700-37 can be fitted throughout by a curve derived from a velocity function of the form of equation (1.1).

In Section 2 we describe the observations and data reduction. Section 3 presents our interpretation of the results in terms of the circumsource and interstellar environment, and the implications concerning stellar winds and the properties of interstellar grains. Section 4 is a summary.

2. OBSERVATIONS AND DATA ANALYSIS

We observed 4U 1538-52 from 1988 February 29 to March 3 with the LAC gas proportional counters of the *Ginga* satellite X-ray observatory. The observatory has been described by Makino et al. (1987) and details of the LAC detector by Turner et al. (1989). The LAC had a 1.1°x2.0° FWHM field of view and an effective area of 4000 cm^2. Pulse height distributions (PHDs) were recorded with various time resolutions from 0.5 to 16 s in 48 channels and channel widths equivalent to 0.58 keV from 0 to 18.6 keV and 1.16 keV from 18.6 to to 37.2 keV. The energy resolution of the LAC detector was 20% FWHM at 5.9 keV. The energy to pulse-height transfer function is represented by a response matrix of 48x700 elements G_{ji} that specify the probability that a photon of energy E_i traversing the effective area of the LAC detector will produce a pulse registered in the jth channel.

Discovery in these data of a cyclotron absorption line centered at 20 keV has been reported previously (Clark et al. 1990). Here we describe our analysis of the eclipse phenomena. To avoid complications in the spectrum arising from the cyclotron resonance we confine the present analysis to the data in channels ≤ 26 (corresponding to energies ≤ 15 keV) which carry most of the information regarding the attenuation and scattering of the X-rays by the atmosphere of the primary. Values of the system parameters of 4U 1538-52 assumed in our analysis are summarized in Table 1.

Three adjustments were made to each transmitted PHD. Particle-induced background was subtracted according to the algorithm developed by Hayashida et al. (1989) from an analysis of the orbital dependence of the background rate. Next we subtracted the contribution of the diffuse cosmic X-ray background from the galactic ridge which was assessed as the PHD (corrected for particle background) observed when the field of view was shifted 2° at constant b^{II} toward higher l^{II} . This comparison field contains no source in the *HEAO 1* sky survey (Wood et al. 1984) the sensitivity limit of which (~0.001 cts cm^{-2} s^{-1}) is approximately 2% of the average uneclipsed counting rate of 4U1538-52 in the same energy range. Finally, to reduce the contribution from X-rays that did not come directly from the neutron star we subtracted the average deep-eclipse PHD from the background-corrected PHDs. Since the average eclipse intensity is only about 2% of the average uneclipsed intensity this correction has a significant effect only on the PHDs observed during the eclipse transitions. In view of the uncertainty as to whether there are fainter undetected sources in the diffuse background comparison field, we cannot be sure that our eclipse PHDs, whose intensities are of the order of 2% of the uneclipsed intensities, have been accurately corrected for diffuse background.

Nevertheless, the similarity of the uneclipsed and eclipsed PHDs above 4.5 keV, and a small systematic change in the spectrum observed over the duration of the eclipse are evidence that the background-subtracted PHDs obtained by this procedure are produced primarily by the eclipsed 4U 1538-52.

2.1. *Variation of the Intrinsic Source Spectrum with Pulse Phase*

Derivation of information about column densities along the lines of sight traversed by the X-rays observed at various orbital phases is complicated by the fact that the energy spectrum varies with pulse phase. To circumvent this problem we derived for each data accumulation interval a nominal average source spectrum according to the following scheme. We first compiled the average pulse phase-resolved PHD for each of sixteen equal intervals of pulse phase from data recorded out of eclipse between orbital phases 0.28 and 0.45 when the attenuation appears to be steady and near its minimum value. For the record, but as a side issue, we characterized these data by fitting to each pulse-phase resolved PHD in channels 7 to 26 (3.5-15 keV) a computed PHD derived as a convolution of the LAC response matrix and a spectrum of the form

$$\begin{aligned} I(E) &= I_0 \exp(-\sigma N_H) E^{-\alpha_1} && E < E_1 \\ &= I_0 \exp(-\sigma N_H) E_1^{-\alpha_1} (E/E_1)^{-\alpha_2} && E_1 < E < E_c \\ &= I_0 \exp(-\sigma N_H) E_1^{-\alpha_1} (E/E_1)^{-\alpha_2} \exp\left(-\frac{(E-E_c)}{E_f}\right) && E_c < E \end{aligned} \qquad (2.1)$$

plus a delta function $I_{Fe}\delta(E-6.4\ \mathrm{keV})$ representing the iron line intensity. For σ we used the sum of the Thompson scattering cross section and the photoelectric absorption cross section of cold matter with normal cosmic abundances given by Morrison & McCammon (1983). In a preliminary analysis we found that the fitted values of the column particle density, N_H, cluster around $2.2\mathrm{x}10^{22}$ H-atoms cm^{-2} of cold matter of which ~$1.6\mathrm{x}10^{22}$ H-atoms cm^{-2} is attributable to the interstellar attenuation estimated from the optical extinction of QV Nor, $A_V \approx 7$ mag (Crampton, Hutchings, & Cowley 1978), and the relationship between extinction and column density (Gorenstein 1975). For the sake of uniformity we therefore fixed N_H at the value $2.2\mathrm{x}10^{22}$ H-atoms cm^{-2}. Listed in Table 2 are the values of the seven adjustable parameters and reduced chi-squares of the fits for each of the sixteen pulse-phase resolved intervals. The line labeled UEav lists the fitted parameters for the average uneclipsed PHD derived from the low-attenuation data. (The low values of the reduced chi-squares indicate that the nominal channel-width uncertainty of 1% in the LAC detector is overestimated.)

The average uneclipsed PHD is displayed in Figure 1. The fitted distribution in channels 7 through 26 is shown as the solid-line histogram. The extension of the fitted PHD below channel 7, based on the same energy spectrum parameters and N_H=$2.2\mathrm{x}10^{22}$ H-atoms cm^{-2} of cold matter, is indicated by the dashed portion of the histogram. The unattenuated average X-ray energy flux from 1 to 15 keV implied by the parameters listed in Table 2 is $7.7\mathrm{x}10^{-10}$ erg cm^{-2} s^{-1}, and the corresponding source luminosity for an assumed distance of 5.5 kpc is $2.8\mathrm{x}10^{36}$ erg s^{-1}. The difference between the dashed histogram and the observed counting rates in the channels below 7 constitutes what we will call the "soft excess" in the uneclipsed spectrum. We will show below that it is, at least in part, an effect of the reduction of the absorption cross section at low energies due to ionization of the circumsource matter by X-rays propagating through the wind.

We partitioned all the data into PHDs accumulated from continuous observation intervals of approximately one pulse period (~530 s), or less if the observation was interrupted by earth occultation, trapped radiation, or other causes. For each accumulation interval we synthesized a nominal low-attenuation PHD as a weighted average of the phase-resolved PHDs, with weights proportional to the exposure times in each of the sixteen pulse phase intervals. To each of these nominal low-attenuation PHDs in channels 7 to 26 we fitted a computed PHD derived as a convolution of the LAC response matrix and equation (2.1) with N_H again fixed at 2.2×10^{22} H-atoms cm^{-2}. The resulting sets of energy spectrum parameters with N_H set equal to zero were taken to represent the unnormalized nominal average source spectra for the various accumulation intervals.

In the final step toward a determination of the nominal source spectra, we fitted to each accumulated PHD in channels 7 to 26 a computed PHD obtained by convolving the LAC response matrix with an energy spectrum derived from the unnormalized nominal average source spectrum. In this fitting we adjusted only the nominal column density N_H' of cold matter, the normalization factor I_0', and the intensity, I_{Fe}', of the fluorescent iron line at 6.4 keV. The other five parameters of the unnormalized nominal source spectrum for that interval were held constant. For $\sigma(E)$ we used the absorption cross section for cold matter and reserved for later a more realistic approach that takes into account the effects of X-ray ionization of the circumsource matter. Plots of the fitted parameters against orbital phase are displayed in Figure 2: N_H' in the top panel of Figure 2; I_{Fe}' in the middle panel; and the ratio I_0'/I_0, representing fluctuations in the source luminosity relative to the synthesized average source spectra, in the bottom panel.

2.2. *Variation with Orbital Phase of the Column Density in the Line of Sight.*

The sharp increases of N_H' near orbital phases −0.1 and 0.1 mark the ingress and egress of the X-ray eclipse. The high values of the column density at orbital phases just before ingress and from 0.50 to 0.60 indicate the presence of density enhancements that may be caused by the effects of X-ray ionization on the radiation-driving mechanism of the stellar wind. In numerical simulations of a stellar wind disrupted by passage of companion X-ray source, Blondin et al. (1990) assumed that the driving mechanism is effectively turned off in the region where $\log\xi > 2$ for lack of ions with resonance absorption lines in the UV. In this region the wind coasts, causing pileup and turbulence near the boundaries and enhanced density in the region beyond. The line of sight to the X-ray source apparently passed through the resulting density enhancements before and during ingress. Since this obscures the density structure of the free-flowing wind, we focused our attention on the data recorded during egress in our analysis of the density profile of the wind, but considered the effects of the density enhancements in our subsequent analysis of the eclipse data.

Figure 3 is a plot of column density against orbital phase during the eclipse egress. The earliest and largest value plotted is based on data from the first accumulation interval after eclipse that shows a statistically significant counting rate above the eclipse level. It is plotted at the orbital phase 29.4° corresponding to the midpoint of the accumulation interval. There is a data gap preceding that interval. Considering the trends of the counting rates and the values of column density derived from the spectrum shapes near the start of egress, we conclude that the emergence from eclipse would have been detected in a preceding accumulation interval if there had not been a data gap. We therefore put the start of egress at orbit phase 28.3°±0.5°.

We tested whether a power-law particle density function derived from equation (1.1), namely

$$n(r) = \frac{\Psi}{4\pi\mu r^2}\left[v_0+(v_t-v_0)(1-r_0/r)^{\beta}\right]^{-1}, \quad r>r_0, \tag{2.2}$$

yields a satisfactory fit of calculated column densities to those displayed in Figure 3. In this function $\Psi = \dot{M}/v_t$ is the ratio of the mass-loss rate to the terminal velocity of the wind, and r_0 is fixed at $0.97\text{x}10^{12}$ cm, which is the stellar radius implied by the eclipse angle of 28.3° and the parameters listed in Table 1. Integrating the density defined by equation (2.2) along the various lines of sight corresponding to the orbital phase of the midpoints of each integration interval, we obtained values of the predicted column densities which were adjusted by changing the parameters Ψ, β, and v_0 to achieve a least-squares fit to the measured values. The fitted function is shown in Figure 3 as a dashed curve with the parameters listed in Table 3. The fitted value of β, namely 2.19, is well outside the range of values (0.5-1.5) that have been used to approximate steady state solutions. The effect of $\beta>1$ is to eliminate the singularity of the acceleration at $r=r_0$, thereby causing a more gradual increase in velocity and a corresponding less rapid decrease in the density, as demanded by the data. Even with this extreme value of β the initial decrease of the power-law density function does not match the data well.

A substantially better fit is obtained with an exponential function of the form

$$n(r) = n_1 \exp\left[-\frac{(r-r_1)}{h}\right], \tag{2.3}$$

where h is a scale height. The exponential function implies a slower initial acceleration, but a velocity that increases without limit as $r \rightarrow \infty$. Therefore we terminate the exponential function at an adjustable radius r_1 and join it smoothly to a function of the form of equation (2.2) with $v_0=0$. The resulting "hybrid" trial density function is represented by equation (2.2) from large distances down to r_1, and by equation (2.3) below r_1 with

$$n_1 = \frac{\Psi}{4\pi r^2 \mu}\left(1-\frac{r_0}{r_1}\right)^{-\beta}. \tag{2.4}$$

As before we fix $r_0 = 0.97\text{x}10^{12}$ cm, so this density function has four adjustable parameters: Ψ, r_1, h, and β. It yields a substantially better fit to the egress data, as can be seen in Figure 3 where it is drawn as a solid line. The parameter values are listed in Table 3.

2.2. *Global Fit of the Density Functions to the Egress Spectra*

The above analysis of the column density variation is deficient in its neglect of the effects of X-ray ionization and heating on the absorption cross sections of the material through which the X-rays pass. To remedy this, we sought a wind model that yields a global fit of calculated PHDs, derived from the nominal source spectra, to all sixteen of the accumulated PHDs from the period of the eclipse egress. We computed the effects of X-ray ionization and heating on the absorption cross sections according to the XSTAR code based on theoretical work of Kallman & McCray (1982) and Krolik & Kallman (1984) and kindly given to us by T. Kallman (private communication). The code computes the absorption cross sections for matter with normal cosmic abundances under the assumption of local thermal and ionization equilibrium for a wide range of conditions of density and X-ray illumination in the approximation of one-dimensional forward propagation. It yields the absorption cross section $\sigma(\xi,E)$ as a function of energy E for a specified X-ray spectrum and a range of densities and X-ray intensities characterized by the ionization parameter

$$\xi = \frac{L_X}{nd^2} , \tag{2.5}$$

where L_X is the X-ray luminosity of the source in the energy range from 13.6 eV to 13.6 keV, d is the distance from the source, and n is the local particle density. With the XSTAR code we computed the photoelectric cross sections for various ionization parameters as shown in Figure 4. To illustrate the effect of X-ray ionization on the propagation of an X-ray spectrum through matter near the X-ray source we computed the attenuation of a simple power law spectrum in passage through a column density of 1×10^{22} H-atoms cm^{-2} with $\log\xi = 0.0$ and 2.0. The emergent spectra are shown in Figure 5 where the relative transparency of the ionized matter below 3 keV is evident.

We fitted calculated PHDs simultaneously to all sixteen PHDs recorded during the egress by adjusting the four parameters of the trial density function. For this global fitting procedure we employed an iterative least-squares code that starts each successive iteration with the sixteen nominal source spectra computed with the updated set of density function parameters and propagates each one step-by-step through the atmosphere along the corresponding line of sight, computing at each step the absorption according to the cross section for the local value of the ionization parameter. The latter depends on the local flux of X-rays which depends, in turn, on the amount of attenuation that has occurred up to that point. We assumed the initial value of L_X/d^2 was $4.0 \times 10^{36}/d^2$ erg s^{-1}. At each step we evaluated ξ from the local attenuated value of L_X/d^2, and derived the local absorption cross sections by interpolation of the data displayed in Figure 4. Beyond 20 stellar radii an additional interstellar attenuation was computed for a constant column density of 1.6×10^{22} H-atoms cm^{-2} of cold matter. The final attenuated spectrum for each data accumulation interval was convolved with the LAC response matrix to obtain a trial PHD that was compared with the data to compute improved values of the density function parameters to be used in the next iteration.

The global fit obtained with the power-law density function of equation (2.2) is displayed in Figure 6 and the fitted parameters are listed in Table 3. Here, as before, the parameter β is forced by the data to a large value, in this case 2.91, by the necessity to fit the power-law function to a much more gradual initial decline with radius than is predicted by steady-state theories. With this value of β, well outside the conventional range for representations of steady state theory, the power-law density function resembles the exponential portion of the hybrid function in the critical range of the fit from $r=r_0$ to $r=1.3r_0$.

Figure 7 shows the global fit obtained with the hybrid density function represented by equations (2.2) and (2.3) joined smoothly at $r=r_1$. The best-fit parameters of the global fits are summarized in Table 3. The exponential portion of the hybrid density function, which implies a less rapid initial acceleration of the wind, achieves a significantly better fit to the data for large column densities, and a substantial improvement in the reduced chi square value of the overall fit. The zero value of the fitted β for the outer ($r>r_1$) power-law range of the hybrid function implies that the velocity beyond r_1 is constant. (Considering the approximate procedure by which we compensated for intrinsic intensity fluctuations, we cannot expect to achieve a reduced chi-square close to the expectation value of 1.0 for a fit that deviates only by Poisson fluctuations.)

The fitted power-law and hybrid density functions, defined by the parameters listed in Table 3, are plotted against radius in Figure 8. For values of $r<r_1$ the two functions are nearly identical where they are both forced most strongly to conform to the actual average run of the density. Beyond r_1 the two functions diverge, with effects on the fits that can be seen in the panels of Figures 6 and 7 for orbital phase greater than 0.1437 where the power law predicts less absorption than the hybrid function.

Figure 9 displays contours of constant $\log\xi$ in the wind described by the globally fitted hybrid density function and irradiated by X-rays emitted by the source with the intrinsic source spectrum derived from the average uneclipsed low-attenuation PHD. The straight lines are the lines of sight at the midpoints of each of the sixteen accumulation intervals during egress.

2.3. *Monte Carlo Computation of X–Ray Propagation*

We developed a Monte Carlo code to compute the propagation of X-rays in three dimensions through an X-ray ionized atmosphere with the aim of obtaining for any specified atmosphere a transfer matrix which could be convolved with a given source spectrum to obtain a prediction of the spectrum of X-rays emerging in any specified direction. Initially we assumed the density in the atmosphere is defined by the globally fitted hybrid density function and the distribution of the ionization parameter values displayed in Figure 9. The code employs the absorption cross sections displayed in Figure 4, and it takes account of Compton scattering, photoelectric absorption, and fluorescent emission from iron and lower Z elements with normal cosmic abundances. The code launches X-ray photons of a specified energy from the neutron star in directions uniformly distributed among $\sim 10^4$ equal $2°\text{x}2°$ elements of solid angle over the entire sphere. Each photon is tracked in steps of one-tenth or less of a mean interaction length. At each step a photon has a chance to suffer a Compton scattering resulting in a change of direction and a small reduction in energy, or a photoelectric absorption with the possible emission of a fluorescent X-ray photon. The code tabulates the exit directions and energies of the photons in the same $\sim 10^4$ elements of solid angle. The resulting tabulations constitute, in effect, the desired transfer matrix to map a given spectrum of X-rays emitted isotropically by the neutron star into the spectrum of transmitted and scattered X-rays that would be observed at a distant point in any given direction. A run consisted of 500 photons at each of 40 energies from 0 to 70 keV in each of the $\sim 10^4$ directions.

Figure 10 displays the results of the Monte Carlo computation for 3 keV and 10 keV X-rays. The solid lines trace the fractional yield of scattered X-rays as a function of orbital phase at an inclination angle of 70°. The dashed line in the 10 keV plot shows the fractional yield of iron fluorescent X-rays. The plots show that the X-ray albedo of the primary star due to source photons of 10 keV is about 4 percent in the range of orbital phase from which we took our low-attenuation data.

The question arises as to whether the Monte Carlo spectrum computed for the orbital phase range from 0.28 to 0.45 accounts for the soft excess defined in section 2.1 as the difference between the observed PHD and the PHD computed from an extrapolation of the spectrum, equation (2.1), fitted to the data in the pulse-height channels above 7. The difference is seen in Figure 11a which is Figure 1 replotted with a linear counting rate scale. We applied the Monte Carlo transfer matrix to the average source spectrum UEav defined in Table 2 with N_H=0 and with I_0 reduced by 4 percent to correct for the presence of albedo in the PHD from which it was derived. The resulting spectrum was reduced by interstellar attenuation in cold matter with a column density of $1.6\text{x}10^{22}$ H-atoms cm^{-2}, and then convolved with the LAC response matrix. The predicted PHD is plotted in Figure 11b together with the observed PHD. The improved fit is evidence that some of the soft excess in the uneclipsed spectrum is a consequence of the relatively larger reduction of the absorption cross section at low energies by X-ray ionization.

The average PHD of X-rays observed in eclipse between orbit phase –0.067 and +0.067 is shown in Figure 12. The X-ray energy flux observed is about 10^{-4} times the bolometric flux of the primary, QV Nor, which is still two orders of magnitude larger than the L_X/L_{bol} ratios typical of the corona of isolated O and B0 supergiants (Cassinelli et al. 1981). We have assumed, therefore, that the contribution of coronal X-rays to the eclipse spectrum is negligible. We applied the Monte Carlo-derived transfer matrix to the average uneclipsed source spectrum as before, this time to predict the deep eclipse spectrum recorded between orbit phase –0.067 and +0.67. The resulting spectrum was reduced by interstellar attenuation in cold matter with N_H=$1.6\text{x}10^{22}$ H-atoms cm^{-2}, and then convolved with the LAC response matrix to obtain the predicted PHD of X-rays scattered into the umbra. The latter is shown as the dashed line in Figure 12. Above channel 8 it is similar in form to the observed distribution, but only ~2/3 of the observed counting rate. We conclude that there is a substantial contribution to the eclipse spectrum by X-rays scattered from circumstellar matter other than that described by the spherically symmetric hybrid density function which we fitted to the eclipse transition data, though we cannot exclude the possibility that some portion of the discrepancy is due to a fluctuation in the luminosity of the source which may have occurred during the eclipse.

Density enhancements, the presence of which is indicated by the increases in column density before ingress and near orbit phase 0.5, are likely sources of additional scattered intensity. Therefore, to the previous density distribution we added an enhancement in a 3-D configuration suggested by the 2-D hydrodynamical calculations of Blondin et al. (1990) which show the effects of X-ray ionization in shutting off the radiation pressure that drives the wind, leaving it to coast where the X-ray intensity is highest. The result is a region of turbulent flow with decreased average velocity and corresponding enhancements of the local density. After some adjustment of the parameters of this model of the enhancement, we obtained a configuration that 1) intersects the orbital plane in a pattern that resembles the non-steady density patterns displayed by Blondin et al., 2) yields predicted curves of counting rates versus orbital phase at various energies that resemble the light curves observed as shown in Figure 13, and 3) predicts a deep eclipse PHD that conforms in shape and magnitude with the observed eclipse PHD in channels ≥ 8 (≥ 4.5 keV). The plot of hardness ratio in Figure 13 confirms that the intensity minima at orbital phases -0.20 and +0.55 are caused by absorption, while the other intensity fluctuations are intrinsic to the source. The intersection pattern of the density enhancement in the orbital plane is indicated in Figure 9, and the resulting predicted deep eclipse spectrum is shown as a solid line in Figure 12.

In channels 8 and below, corresponding to energies less than 4.5 keV, the Monte Carlo calculation predicts rates well below the observed rates in eclipse. By subtracting the Monte Carlo distribution we obtain the PHD shown in Figure 14 which we attribute to a "soft component" that may consist of X-rays scattered by interstellar grains and/or thermal emission by hot and uneclipsed circumsource matter.

3. DISCUSSION

3.1 *Density Function of the Radiatively-Driven Wind.*

The values of $\Psi = \dot{M}/v_t$ listed in Table 3 exhibit the differences between the physical implications of the fits obtained with the power law and the hybrid density functions. When the power law function is fitted to the derived column density data or used in the global fit to the PHD's, smaller values of $\dot{M}/v_t$ are obtained due to the rapid decline of the power law function and the need to conform to the data of high statistical weight at large radii. The relatively smaller fitted values of $\dot{M}/v_t$, obtained from fits in which the effects of X-ray ionization are ignored, show the effects of underestimating the density due to the use of absorption cross sections of unionized matter.

Rayleigh-Taylor instability in the winds of early-type stars, suggested by Lucy & Solomon (1970), and discussed by various authors (e. g., Nelson & Hearn 1978; MacGregor, Hartmann, & Raymond 1979; Lucy & White 1980; Lucy 1982, 1984; Krolik & Raymond 1985) causes turbulence and localized shock heating of coronal gas in both the subsonic and supersonic regions and is the likely source of the ubiquitous soft X-ray emission of early-type stars. Thus a density profile derived from an analysis of

X-ray absorption during an eclipse transition must be considered an average over an inherently non-steady density distribution.

Poe, Owocki, & Castor (1990) explored the solution topology of an equation describing the acceleration of a radiatively-driven wind without the Sobolev approximation. They find the solutions are intrinsically unstable for realistic values of v_{th}/v_a, the ratio of the ion thermal speed to the sound speed. By setting this ratio to the unrealistic value 0.5 they obtain a stable solution for a star of radius $1.4\text{x}10^{12}$ cm which they find "corresponds to the asymptotic state approached for unperturbed models in the time-dependent simulations." They suggest that real absorption line-driven winds, more realistically modeled with $v_{th}/v_a = 0.375$, are highly variable, "with both the velocity law and mass-loss rate fluctuating about the allowed steady values" (obtained with $v_{th}/v_a = 0.5$). Their non-Sobolev steady-state solution can be fitted rather well by an exponential density function in the lower region with a scale height of $5\text{x}10^{10}$ cm, with a transition at $1.3r_0$ to a conventional density function with $\beta = 0.5$, and a mass-loss rate $1\text{x}10^{-6}$ $M_\odot$/yr. The similarity in form between their asymptotic density curve and the one we fitted to the eclipse egress data of 4U 1538-52 lends credence to an interpretation of our hybrid density function as an average of a turbulent flow. Perhaps one could achieve a more significant comparison of the theory of unstable flow with X-ray measurements of column density profiles by computing the average density function of many randomized numerical hydrodynamical simulations of unstable flow with $v_{th}/v_a = 0.375$.

3.2. *Properties of interstellar grains inferred from a comparison of the fractional intensity of grain-scattered X-rays and the optical extinction of QV Nor.*

The optical depth τ_s from 4U 1538-52 for scattering of X-rays by interstellar grains is much less than 1 over the energy range of our observation. Assuming that the detected X-rays that have been scattered by interstellar grains and those that arrive directly from the source suffer the same absorption, we can express the fractional intensity of the grain-scattered component as

$$\frac{I_g(E)}{I(E)} = 1 - \exp\left[-\tau_s(E)\right] \approx \tau_s(E) \,. \tag{3.1}$$

Adopting the characterization of interstellar grains as spheres of dielectric material distributed evenly along the path from the source, and expressing the optical depth as the product of the density of the grains, their scattering cross section, and the distance D of the source, the fractional intensity of grain-scattered X-rays can be written as

$$\frac{I_g(E)}{I(E)} = D\pi \int Q_s(x_E) a^2 n_g(a) da \,, \tag{3.2}$$

where $Q_s(x_E)$ is the scattering efficiency of the grains for photons of energy E by grains of radius a,

$x_V = (2\pi aE/hc)$, and $n_g(a)da$ is the average density of grains with radii between a and $a+da$. The total optical extinction in magnitudes caused by the same population of grains is

$$A_V = 1.086\pi D \int Q_e(x_V) a^2 n_g(a) da \,, \tag{3.3}$$

where $Q_e(x_V)$ is the extinction efficiency factor and $x_V = 2\pi a/\lambda_V$ with $\lambda_V = 5550$ Å (Spitzer 1978). We now call $R_{XV}(E)$ the ratio of the fractional intensity of grain-scattered X-rays of energy E to the total extinction,

$$R_{XV}(E) = \frac{I_g(E)}{A_V\, I(E)} \,. \tag{3.4}$$

According to equations (3.2) and (3.3) the expected value of this ratio in reciprocal magnitudes for a given grain model characterized by Q_{sca}, Q_e, and n_g is

$$R_{XV}(E) = \frac{\int Q_s(x_E) a^2 n_g(a) da}{1.086 \int Q_e(x_V) a^2 n_g(a) da} \tag{3.5}$$

A comparison between measured and expected values of R_{XV} tests the validity of the model.

In the Rayleigh-Gans approximation the scattering efficiency of a spherical particle of radius a for X-rays of energy E is (van de Hulst 1981)

$$Q_s(x_E) = 2(r_e N h c a)^2 E^{-2} \,, \tag{3.6}$$

where N is the electron density in the grain, and r_e, h, and c, are the electron radius, Planck's constant and the speed of light, respectively. In terms of the specific density ρ, the mean mass number M, and the mean atomic number Z, the electron density is $N = \rho(Z/M)N_A$ where N_A is Avagadro's number. The approximation is valid for $a \ll 0.5\,(E/\rho)$ µm, where E is in units of 1 keV. We note that the counts we attribute to the soft component of the eclipse spectrum shown in Figure 14 are concentrated in the channels corresponding to calibration energies in the range from ~2 to 4 keV. We can therefore use the Rayleigh-Gans approximation in an analysis of the implications of the grain-scattered X-ray intensity for the properties of interstellar grains with radii less than $1.0/\rho$ µm.

Combining equations (3.5) and (3.6), evaluating the constants, and expressing a in units of 0.1 µm and E in keV, we obtain for the expected value of $R_{XV}(E)$ in reciprocal magnitudes the equation

$$R_{\mathrm{XV}}(E) = 0.184 \left(\frac{2Z}{M}\right)^{2}\left(\frac{\rho}{3}\right)^{2} \frac{\int a^{4} n_{\mathrm{g}}(a)da}{\int Q_{\mathrm{e}}(z_{\mathrm{V}})a^{2} n_{\mathrm{g}}(a)da} E^{-2}. \tag{3.7}$$

If we set $Q_{\mathrm{e}}=2$, and assume the distribution function is a delta function at a grain radius of 0.1 μm, we obtain a formula equivalent to that derived by MG for the ratio of the fractional halo intensity to the total extinction. They determined values of this ratio by dissecting images of X-ray stars recorded by the *Einstein* observatory and found the results to be generally consistent with the prediction of their formula for a model of grains with mixed compositions of silicates and graphite, a mean specific density of 3, and a mean radius of 0.1 μm. However, $Q_{\mathrm{e}}< 0.5$ for spherical dielectric grains with $a \leq 0.1\mu\mathrm{m}$. Thus the predicted ratio of grain-scattered X-ray intensity to optical extinction for such a grain model is actually substantially larger than the estimate of MG and, in fact, very much larger than the X-ray data allow, as we shall show. The present formulation enables a more interesting conclusion to be drawn about the properties of interstellar grains from a comparison of optical extinction and X-ray scattering.

During an eclipse of an X-ray binary the intensity of X-rays that arrive directly from the binary system is greatly reduced. What remains of the direct intensity are X-rays that have been scattered or radiated into the umbra from the circumstellar matter plus the much fainter X-rays from the primary itself. However, as pointed out earlier, the intensity of grain-scattered X-rays persists due to the additional travel times along deflected paths. As these X-rays straggle in, their intensity decays. At time t after ingress the surviving fraction of the intensity, $I_{\mathrm{g}}(t)/I_{\mathrm{g}}(0)$, can be estimated as the integral from t to infinity of the probability per unit time that a single-scattered photon has suffered a delay t'. Using the approximate formula for this probability given by Alcock & Hatchett (1978) for the case of grains distributed uniformly along the path, and adjusting the coefficients of the exponentials to obtain unity at $t=0$, we express the surviving fraction as

$$I_{\mathrm{g}}(t)/I_{\mathrm{g}}(0) = 0.90 \exp(-t/t_{\mathrm{g}})+0.10 \exp(-6.8t/_{\mathrm{g}}), \tag{3.8 }$$

where

$$t_{\mathrm{g}} = 0.71\left(\frac{hc}{2\pi aE}\right)^{2}\frac{D}{2c} \approx 40\, a(0.1\ \mu\mathrm{m})^{-2}E(\mathrm{keV})^{-2}D(\mathrm{kpc})\ \mathrm{hrs}. \tag{3.9}$$

The expected effects of post-ingress decay on the spectrum of grain-scattered X-rays are shown in Figure 15. The displayed spectra were computed according to equation (3.9) as averages over the first and the second halves of the eclipse from orbital phase −0.07 to +0.07 for grain radii 0.01, 0.03 and 0.1 μm. The spectrum at $t=0$ was assumed to be the average uneclipsed spectrum with the parameters listed in Table 2, multiplied by E^{-2} in accordance with the theoretical energy dependence of the scattering efficiency. The corresponding ratios of the calculated average total counting rates in the second half to the first half of the eclipse in channels 3 through 7 (calibration energies from 1.1 to 3.9 keV) are 0.97, 0.82, and 0.52. Thus a substantial decrease is expected during the eclipse in the rate of X-rays that have been scattered by grains larger than 0.03 μm. However, the observed ratio was 1.15±0.05, which implies that not all of the soft component is grain-scattered, and assures that an estimate of R_{XV} based on the average PHD of the soft component in the first half of the eclipse will be a conservative upper bound on the true value.

To estimate this upper bound on R_{XV} we note first that the uneclipsed X-ray intensity of 4U 1538-52 shows little variation when averaged over periods of several thousand seconds in our ~3.5-day data set displayed in Figure 1, and over several hours in the accumulated 0.5-day observations by *EXOSAT* (Orlandini 1990). We therefore adopt the average uneclipsed spectrum with the parameters listed in Table 2 as the source spectrum $I(E)$ in equation (3.4). According to equation (3.4) and (3.7) the quantity

$$E^2 R_{XV}(E) = \frac{I_g(E)}{A_V E^{-2} I(E)} \tag{3.10}$$

is a constant that depends only on the grain model. Therefore, the expected spectrum of grain-scattered X-rays can be represented as

$$I_g(E) = k_s E^{-2} I(E)\ , \tag{3.11}$$

where k_s is a constant to be determined from the X-ray data. We fitted the PHD implied by this function to the average PHD of the soft component recorded during the first half of the eclipse by adjusting k_s to the value 0.12±0.01. The measured color excess $E(B-V)$ of QV Nor is ~2.2 mag (Crampton, et al. 1978). Therefore A_V, the interstellar extinction at the visual wavelength, 5550 Å, may be assumed to lie in the range 6.4 mag$<A_V<$7.5 mag, where the width of the range reflects the uncertainty in the ratio $A_V/E(B-V)$. Dividing k_s by the lower limit on A_V, we find

$$R_{XV}(E{=}2\ \mathrm{keV}) \leq (0.0047 \pm 0.0004). \tag{3.12}$$

This can be compared with the results derived by MG from an analysis of X-ray images recorded by the *Einstein* observatory. They determined the fractional halo intensities of six X-ray stars for which values or limits on the total extinction A_V of their optical counterparts were known. The linear relation which they fitted to their plot of the fractional halo intensity against A_V can be represented by the formula

$$R_{XV}(E{=}1\ \mathrm{keV}) = 0.012 + 0.043/A_V\,. \tag{3.13}$$

Substituting A_V=6.4 mag, this formula yields $R_{XV}(E=1 \text{ keV})=0.019$, which is equivalent to 0.019/4=0.0047 at E=2 keV, in agreement with the upper bound we have derived from the eclipse data of 4U 1538-52.

We examined the compatibility of our upper bound on R_{XV} with values calculated for a model of interstellar grains as homogeneous dielectric spheres with $(2Z/M)=1$, a complex index of refraction $m=1.3-0.09i$, a specific density of 3, and a size distribution of the form used by Mathis, Rumple, & Nordsieck (1977, hereafter MRN)

$$n_g(a) \sim a^{-p} \quad , \quad a_1 < a < a_2 . \tag{3.14}$$

The optical extinction efficiency, computed according to the formulas for spheres with a refractive index near 1 given by van de Hulst (1981), is plotted against the grain radius as the solid curve labeled 'a' in Figure 16. In the same figure the X-ray scattering efficiency (eq. [3.6]) is plotted as the dashed curve labeled 'a'. In Figure 17 the curve labeled 'a' is a plot of $R_{XV}(E=2 \text{ keV})$ for a population of such grains against the upper limit a_2 of their size distribution with a_1=0.001 μm and p=3.7. The upper bound, indicated by the horizontal line, is exceeded for a_2>0.005 μm. Grain models that account for optical extinction curves require size distributions that extend well beyond this value. For example, MRN found that interstellar extinction over the wavelength range 0.11 μm < λ < 1 μm can be fitted by grains composed of a variety of refractory substances with the size distribution of equation (3.10) within the limits a_1=0.005 μm to a_2=1 μm. This gross discrepancy between the size limit imposed by the X-ray data and the size range required to satisfy optical extinction data implies that interstellar grains of a given size are much less efficient as X-ray scatterers than predicted on the assumption that they are compact with densities typical of silicates. Since the X-ray scattering efficiency varies as ρ^2, the likely explanation is that the average density of interstellar grains is much less than that of solid silicates. Consider, then, the extinction and scattering properties of compact grains with the same refractive index as before, but with a density $\rho \sim 1.0$ as in ice. The curves for ice spheres are labeled 'b' in Figures 16 and 17. Here the upper bound on R_{XV} is exceeded for a_2>0.1 μm, which is still uncomfortable small. Moreover, grains of pure solid ice are not a realistic possibility.

If, instead of being compact, interstellar grains are "fluffy", i.e., loose aggregates of small solid particles as discussed by Mathis & Whiffen (1989), then grains of a given size may have much smaller values of R_{XV} than compact grains of the same size and chemical composition. Such aggregate grains have been observed in interplanetary dust collected at high altitude by Bradley, Humecki, & Germani (1992). Mathis & Whiffen computed the extinction curves of aggregate grains composed of particles of silicate, amorphous carbon and graphite stuck together in loose aggregates with as much as 80% of the grain volume empty. They estimated the effective complex dielectric constant $\varepsilon_{\rm eff}$ of a loose aggregate of such particles with several different complex dielectric constants ε_i occupying various fractions f_i of the grain volume by the Bruggeman rule which requires the solution of the polynomial equation

$$\sum_i f_i \frac{\varepsilon_i - \varepsilon_{eff}}{\varepsilon_i + 2\varepsilon_{eff}} = 0. \tag{3.15}$$

To explore the implications of a fluffy grain model for the value of R_{XV} we developed a Monte Carlo program to simulate grain formation by random accretion of spherical particles of uniform size that stick on contact. Each grain was started as a single particle of unit radius and allowed to grow by capture of additional identical particles launched one by one in random directions from random positions on a concentric spherical surface with a radius larger than the final size of the grain. A "filling fraction function" of each grain was assessed as the ratio $f(\alpha)$ of particle volume to total volume inside a fiducial sphere of radius α concentric with the final center of mass of the grain. Figure 18 is a plot of the average of the filling fraction functions for ten one-thousand-particle grains against α measured in units of the particle radius. The dotted lines indicate the rms deviation from the average. We take the value at α=10 particle radii where f=0.205±0.008 as the average filling fraction and rms deviation in the interior of model grains of all sizes grown in this manner. We note that this value of f is essentially the same as that used by Mathis &Whiffen in their discussion of aggregate grains.

The curves labeled 'c' in Figures 16 and 17 are the calculated extinction and scattering efficiencies and R_{XV} for fluffy grains composed of particles with the same index of refraction as the dielectric previously considered, a filling factor of 0.205, and a specific density of 1.2. The effective index of refraction of the grains for visible light $m_{eff}=(\varepsilon_{eff})^{1/2}$ was computed by the Bruggeman rule. The X-ray scattering efficiency was calculated as before, but with the average density of the grains set equal to f times the density of the constituent particles. From the plot one can see that a model of aggregate grains with a filling fraction of ~0.2, an MRN size distribution with p=3.7 and a_2=0.3 μm, and composed of particles with a refractive index m=1.3-0.09i and a specific density of 1.2 is compatible with the measured upper bound on R_{XV}. One can imagine particles with these properties being composed of a core of silicate and/or graphite with ice mantles, i.e., "dirty ice." Though simplistic, this model serves to illustrate the constraint that X-ray scattering data place on the density and size distribution of interstellar grains.

3.3. Possible contribution of thermal brehmsstrahlung to the soft component in eclipse.

A possible source of a portion of the soft component is thermal emission from the density enhancements which may be caused, as in the simulations of Blondin et al. (1990), by the wind moving with high velocity piling up against coasting X-ray ionized plasma. The solid curve in Figure 13 is the PHD of a thermal brehmsstrahlung spectrum fitted to the data by adjustment of the intensity and the temperature. The fitted value of the temperature is 5.0×10^7 K, and the fitted intensity, if isotropic, implies a luminosity 5.3×10^{34} erg s^{-1} in the 1 to 10 keV band.

One would expect the radiation pressure-driven wind piling up against coasting X-ray ionized plasma near the orbit of the neutron star to be shock-heated to a temperature $T_S \sim 3\mu v_S^2/16k \sim 3.0\times10^7(v_S/1000$ km s$^{-1})^2$ K where v_S is the upstream velocity (McKee & Hollenbach 1980). The total luminosity of a wind with parameters equal to those we fit to the egress data is 3.0×10^{36} erg s^{-1} for a terminal velocity of 2,000 km s^{-1}, so the interception and conversion of only a small fraction of the wind energy would be sufficient to generate the observed soft X-ray component. Thermal emission from the density enhancements is therefore a plausible source of some of the soft component.

SUMMARY

We have explored the implications of the eclipse phenomena of the X-ray binary 4U 1538-52/QV Nor for the stellar wind of the primary and the properties of interstellar grains. Our principal conclusions are:

1. The run of density in the atmosphere of QV Nor, the massive B0 I companion of 4U 1538-52, cannot be fitted well by a density function which is derived from the velocity function often used to represent the results of steady-state theories of radiatively-driven winds in the Sobolev approxitmation, namely $v(r)=v_0+v_t(1-r_0/r)^\beta$, with β in the range from 0.5 to 1.5. The density function can be fitted much better by a hybrid function in the form of an exponential function of radius with a scale height of 4.5×10^{10} cm in the inner region out to a radius of $1.22 r_0$, joined smoothly to a power law function at a point where the velocity reaches its terminal value. This result, like similar results obtained from eclipse observations of some other X-ray binaries, adds to the evidence that steady-state theories do not provide an accurate description of radiatively-driven winds. The hybrid density function that we fit to our data must be considered as an approximate representation of the average density in an inherently turbulent flow.

2. The pulse-height distribution (PHD) of X-rays observed in eclipse in pulse-height channels corresponding to energies above 4.5 keV can be fitted by a calculated distribution derived by a Monte Carlo computation of Compton scattering and fluorescence by matter with the average density described by the hybrid function derived from analysis of the X-ray attenuation during egress plus density enhancements caused by X-ray ionization effects on the wind flow.

3. Subtraction from the eclipse PHD of the calculated Monte Carlo PHD, normalized to the data above 4.5 keV, leaves a soft component which can be explained in part as grain-scattered X-rays that persist through the eclipse due to transit time delays and in part as thermal brehmsstrahlung from the shock-heated density enhancements.

4. We have derived a constraint on models of the composition and size distribution of interstellar grains in the form of an upper bound on a quantity $R_{XV}(E)$ which we call the ratio of the fractional intensity of grain-scattered X-rays of energy E to the total optical extinction at wavelength 5550 Å. Taking the upper limit on the grain-scattered intensity to be the whole of the soft component of the eclipse spectrum, and the lower limit on the total optical extinction to be A_V=6.4 mag, we find an upper limit of (0.0047±0.0004) on R_{XV}(2 keV) expressed in reciprocal magnitudes. This limit is grossly incompatible with a model of compact spherical dielectric grains with a specific density of ~3 and a size distribution that extends to the sizes greater than 0.1 μm which are required to explain optical extinction curves. However, our upper limit on R_{XV} is consistent with a model of "fluffy" grains in the form of

spherical aggregates of smaller particles that occupy ~20% of the grain volume and have a refractive index like that of "dirty ice" and a specific density of ~1.2.

ACKNOWLEDGEMENTS

We thank T. Kallman for providing us with the XSTAR code and for his assistance in applying it to our computations, and K. Arnaud for help in installing the XSPEC code on our computer system. GC and JW thank the Institute for Space and Astronautical Science and the ISAS X-ray Astronomy Group for their hospitality during extended visits. We thank the Ginga staff for assistance in the observations and data reduction. We are indebted to an anonymous referee for critical comments that stimulated an extensive revision of the manuscript. This research was supported in part by Grant NAG8-701 from the National Aeronautics and Space Administration.

Table 1. Parameters of the binary system 4U 1538-52/QV Norma.

$l^{\mathrm{II}}=327.4°$ $b^{\mathrm{II}} = 2.1°$

P_{orb}	3.72844 ± 0.00002 days	a
$a_{\mathrm{x}}\sin i$	(1.53±0.11) x 10^{12} cm	a
inclination	~70°	e*
$M_{\mathrm{opt}}/M_{\mathrm{x}}$	16.1±1.2	c
θ_{e} (eclipse half-angle)	28.3°± 0.5°	d
r_0 (primary radius)	(0.97± 0.12) x 10^{12} cm	e
P_{pulse}	530.43 ± 0.014 s	a
L_{x} (1-15 keV)	(2.8±1.5) x10^{36} erg s^{-1}	d
L_{opt}	(6.2±2.0) x10^{38} erg s^{-1}	c
Spectral type	B0 I	b
A_{V}	6.4 - 7.5 mag	b*
distance	5.5 ± 1.5 kpc	b

a. Corbet, Woo, & Nagase (1992)

b. Crampton, Hutchings, & Cowley (1978)

b*. Using $E(B-V)\approx2.2$ mag from ref.b and $A_{\mathrm{V}}/E(B-V)=2.9$-3.4

c. Reynolds, Bell, & Hilditch (1992)

d. This work

e. Derived

e*. Assuming the primary fills 90 percent of its Roche lobe.

Table 2. Values of seven parameters characterizing the sixteen phase-resolved incident spectra derived from data recorded between orbit phases 0.28 and 0.45 and the average (UEav) spectrum. The column density N_H was fixed at the value 2.2×10^{22} H-atoms cm^{-2}. Typical one-sigma errors are quoted for the sixteenth phase-bin spectrum.

Phase bin no.	I_0 photons s^{-1} keV^{-1}	α_1	E_1 keV	α_2	E_c keV	E_f keV	I_{Fe} photons s^{-1}	χ_ν^2
1	137.1	1.14	5.2	1.56	9.0	26.8	1.7	1.14
2	148.9	1.30	9.6	0.66	12.3	8.4	1.7	1.02
3	143.8	1.16	8.0	0.59	13.1	9.8	1.3	1.66
4	169.2	1.23	6.9	0.63	13.2	7.1	2.7	1.22
5	202.4	1.26	7.9	0.84	12.8	8.3	2.0	0.82
6	106.7	0.84	5.1	1.17	12.1	8.8	1.4	0.89
7	154.6	1.37	8.5	1.00	11.7	9.1	1.3	0.55
8	174.6	1.41	4.0	1.73	15.0	0.9	1.3	1.94
9	149.4	1.08	3.5	1.65	13.3	7.1	1.4	1.67
10	477.4	1.62	10.6	-0.76	11.2	4.8	0.5	0.59
11	351.0	1.32	8.8	0.67	11.8	10.9	0.0	1.00
12	328.9	1.25	6.7	0.87	12.1	20.5	2.1	0.82
13	304.2	1.19	6.9	0.76	12.4	21.8	2.4	0.46
14	294.3	1.19	8.3	0.68	14.3	5.6	0.6	0.91
15	475.3	1.50	10.0	0.73	13.3	14.6	0.5	0.92
16	341.2	1.39	5.7	1.64	9.7	19.5	0.3	0.48
±	32.4	0.07	1.5	0.15	0.9	4.9	1.3	
UEav	236.0	1.28	8.9	0.91	12.4	13.7	1.0	0.42
±	19.6	0.04	0.5	0.09	0.5	2.5	0.3	

Table 3. Summary of fitted density function parameters derived as described in the text. Parenthesized quantities were held constant. No meaningful errors could be determined since systematic errors dominate.

density function	column density fits		global spectra fits	
	pwr law	hybrid	pwr law ionized	hybrid ionized
$\dot{M}/v_t$ (10^{-9} $M_\odot$ yr^{-1}km^{-1}s)	0.07	0.28	0.03	1.19
v_0 (km s^{-1})	0		0.4	
r_0 (10^{12} cm)	(0.97)	(0.97)	(0.97)	(0.97)
β	2.19	0.72	2.91	0.0
h (10^{10} cm)		4.69		4.50
r_1 (10^{12} cm)		1.25		1.22
N_H^{ISM} (10^{22} cm^{-2})	(1.6)	(1.6)	(1.6)	(1.6)
χ_ν^2	22	16	8.2	4.6
degrees of freedom	50	48	317	316
fitted parameters	2	4	2	4

REFERENCES

Abbott, D. C. 1980, ApJ, 242, 1183

-------- 1982, ApJ, 259, 282

Alcock, C., & Hatchett, S. 1978, ApJ, 222, 456

Blondin, J. M., Kallman, T. R., Fryxell, B. A., & Taam, R. E. 1990, ApJ, 356, 591

Bradley, J. P., Humecki, H. J., & Germani, M. S. 1992, ApJ, 394, 643

Castor, J. I., Abbott, D. C., & Klein, R. I. 1975, ApJ, 195, 157

Cassinelli, J. P. 1979, ARA&A, 17, 275

Cassinelli, J. P., Waldron, W. L., Sanders, W. T., Harnden, F. R. Jr., Rosner, R., & Vaiana, G. S. 1981, ApJ, 250, 677

Clark, G. W., Minato, J. R., & Mi, G. 1988, ApJ, 324, 974

Clark, G. W., Woo, J. W., Nagase, F., Makishima, K., & Sakao,T. 1990, ApJ, 353, 274

Corbet, R. H. D., Woo, J. W., & Nagase, F. 1992, ApJ, submitted

Crampton, D., Hutchings, J. B., Cowley, A. P. 1978, ApJ, 225, L63

Day, C. S. R., & Stevens, I. R. 1992, ApJ, submitted

Friend, D. B., & Abbott, D. C. 1986, ApJ, 311, 701

Gorenstein, P. 1975, ApJ, 198, 95

Haberl, F., White, N. E., & Kallman, T. R. 1989, ApJ, 343, 409

Hayakawa, S. 1970, Prog. Theor. Phys. 43, 1224

Hayashida, K., et al. 1989, PASJ, 41, 373

Kallman, T.R., & McCray, R. 1982, ApJ S, 50, 263

Krolik, J. H., & Kallman, T. R. 1984, ApJ, 286, 366

Krolik, J. H., & Raymond, J. C. 1985, ApJ, 298, 660

Lewis, W., Rappaport, S., Levine, A., & Nagase, F. 1992, ApJ, 389, 665

Lucy, L. B., & Solomon, P. M. 1970, ApJ, 159, 879

Lucy, L. B., & White, R. L. 1980, ApJ, 241, 300

Lucy, L. B. 1982, ApJ, 255, 286

-------------- 1984, ApJ, 284, 351

Makishima, K., Koyama, K., Hayakawa, S., & Nagase, F. 1987, ApJ, 314, 619

Makino, F., et al. 1987, Ap. Lett. Comments, 25, 223

Martin, P. G. 1970, MNRAS, 149, 221

Mathis, J. S., Rumpl, W., & Nordsieck, K. H. 1977, ApJ, 217, 425

Mathis , J. S., & Whiffen, G. 1989, ApJ, 341, 808

Mauche, C. W., & Gorenstein, P. 1986, ApJ, 302, 371 (MG)

MacGregor, K. B., Hartmann, L., & Raymond, J. C. 1979, ApJ, 231, 514

McKee, C. F., & Hollenbach, D. J. 1980, ARA&A, 18, 219

Mitsuda, K., Takeshima, T., Kii, T., & Kawai, N. 1990, ApJ, 353, 480

Morrison, R., & McCammon, D. 1983, ApJ, 270, 119

Nelson, G. D., & Hearn, A. G. 1978, AA, 65, 223

Orlandini, M. 1990, PhD Thesis, International School for Advanced Studies, Trieste

Overbeck, J. 1965, ApJ, 141, 864

Poe, C. H., Owocki, S. P., & Castor, J. I. 1990, ApJ, 358, 199

Predehl, P., Bräuninger, H., Burkert, W., & Schmitt, J. H. M. M. 1991, A&A,246, L40

Prinja, R. K., & Howarth, I. D. 1986, ApJS, 61, 357

Reynolds, A. P., Bell, S. A., & Hilditch, R.W. MNRAS, 256, 631

Sato, N. et al. 1986, PASJ, 38, 731

Schreier, E., Levinson, R., Gursky, H., Kellogg, E., Tananbaum, H., & Giacconi, R. 1972, ApJ, 172, L79

Spitzer, L. 1978, Physical Processes in the Interstellar Medium (New York: Wiley)

Turner, M., et al. 1989, PASJ, 41,345

van de Hulst, H. C. 1981, Light Scattering by Small Particles (New York: Dover)

Wood, K. S. , et al. 1984, ApJS, 56, 507

FIGURE LEGENDS

Figure 1. Average PHD of X-rays recorded during the orbital phase interval from 0.28 to 0.45 when the attenuation was near its minimum value. The fitted PHD (solid line) is derived from a spectrum of the form of equation (2.1) of the text with the parameter values listed in Table 2 in the row labeled UEav. Extension of the fitted PHD to channels below 7 exposes a soft excess in the uneclipsed spectrum an explanation of which is found in the effects of X-ray ionization on the photoelectric absorption cross section.

Figure 2. Plots of fitted quantities characterizing the X-ray spectra against orbital phase: a) column density of hydrogen atoms; b) iron line intensity; c) intensity fluctuations relative to the synthesized average source spectra.

Figure 3. Column densities derived from spectrum fits plotted against orbital phase, together with fitted column density curves based on the power-law density function and the hybrid density function. The fitted parameters of the density functions are listed in Table 3.

Figure 4. Photoelectric absorption cross sections computed by the XSTAR code for various values of $\log\xi$.

Figure 5. Comparison of the attenuation of a power law spectrum by passage through a column density of 1×10^{22} H-atoms cm^{-2} with values of $\log\xi$ equal to 0.0 (dotted line) and 2.0 (dashed line). The solid line represents the unattenuated spectrum.

Figure 6a,b. Global fits of calculated PHDs derived from the power-law density function.

Figure 7a,b. Global fits of calculated PHDs derived from the hybrid density function.

Figure 8. Comparison of the power-law (dashed line) and hybrid (solid line) density functions derived by the global fit to the eclipse egress data.

Figure 9. Ionization contours for the fitted hybrid density function and a source luminosity of 4×10^{36} erg s^{-1} in the energy range below 13.6 keV. The wrinkles in the contour lines are an artifact of the computation. The lines of sight at the midpoints of each of the intervals for accumulation of the data used in the global fit are indicated by the lines emanating from the source. The intersection pattern of the density enhancement in the orbital plane is shown as the two paddle-shaped figures.

Figure 10. Scattered fraction of X-rays for two launch energies plotted against orbital phase as derived

from the results of the Monte Carlo computation: a) 10 keV - the solid line is the scattered fraction, the dashed line is the fluorescent fraction; b) 3 keV - the solid line is the scattered fraction.

Figure 11. Calculated and observed PHDs in the low-attenuation range of orbital phase from 0.28 to 0.45. The solid line in a) shows the PHD computed from the spectrum fitted to the data in channels above 7 and extrapolated to the lower channels as in Figure 1. The discrepancy in the lower channels is the soft excess. The same data are shown in b), but with the PHD from the Monte Carlo calculation that takes account of the effects of X-ray ionization on the photoelectric absorption cross sections. The improved fit indicates that the soft excess in the uneclipsed spectrum is an effect of X-ray ionization.

Figure 12. Average PHD recorded during eclipse. The dashed line is the PHD predicted by Monte Carlo computation for X-rays with the intrinsic source spectrum that have been scattered from circumstellar matter with the hybrid density function derived in the global fit of the egress data, and reduced by interstellar attenuation. The solid line is the predicted PHD obtained with a density enhancement equivalent in effect to an increase in the wind parameter Ψ by a factor of 1.5 The difference between the observed PHD and the normalized Monte Carlo prediction below 4.5 keV is what we call the soft component of the eclipse spectrum.

Figure 13. Counting rates in various pulse-height channels and hardness ratio plotted against orbital phase. The nominal energy boundaries of the pulse-height channels are indicated. The solid line is the counting rate "light curve" predicted by the Monte Carlo calculation with the ad hoc density enhancements the conspicuous effects of which are the minima around orbital phases −0.2 and +0.55.

Figure 14. Pulse height distribution of the soft component derived by subtracting the Monte Carlo distribution from the average eclipse distribution . The solid line is the predicted distribution that can be attributed to thermal brehmsstrahlung from optically thin plasma at a temperature of 5×10^6 K and a source luminosity of 5.3×10^{34} erg s^{-1}. The dashed line is the predicted spectrum of grain-scattered X-rays adjusted in amplitude to fit the data.

Figure 15. Comparison of the predicted changes in the PHDs of grain-scattered X-rays from the first to the second half of the eclipse for three different sizes of grains. The ratios of the total counting rates in channels 3 through 7 are displayed in the inset table.

Figure 16. Theoretical optical extinction efficiencies Q_e(solid lines) for λ=5550 Å and X-ray scattering efficiencies Q_s (dashed lines) for E=2 keV plotted against radius for three models of spherical grains composed of particles with a refractive index 1.3−0.09i and various combinations of the specific density ρ of the particles and the filling factor f of the grains: a) ρ=3, f=1; b) ρ=1, f=1; c) ρ=1.2, f=0.2. The scattering efficiency curves terminate at $a=1.0(f\rho)^{-1}$ μm beyond which the Rayleigh-Gans

approximation fails.

Figure 17. Calculated values of $R_{XV}(E=2\ \mathrm{keV})$ for various populations of interstellar grains with the MRN size distribution plotted against the upper limit a_2 of the distribution for the three models of interstellar grains referred to in Figure 15. The horizontal line is the upper bound on $R_{XV}(E=2\ \mathrm{keV})$ derived from our data.

Figure 18. Average filling fraction function of ten randomly generated model aggregate grains plotted against radius from the center of mass of each grain, measured in units of the constituent particle radius.

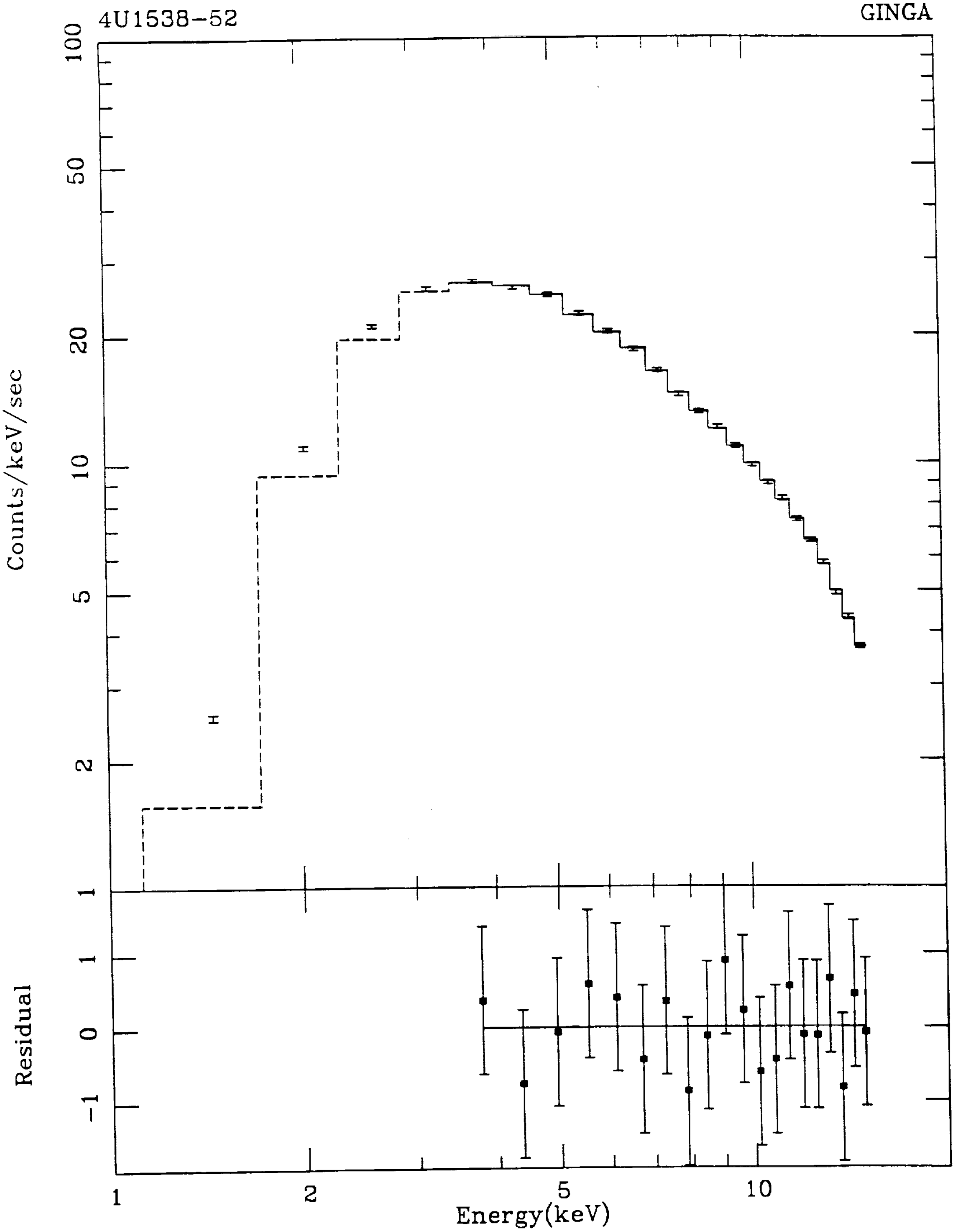
4U1538-52
GINGA
Counts/keV/sec
100
50
20
10
5
2
1
Residual
1
0
−1
1
2
5
10
Energy(keV)

Figure 1

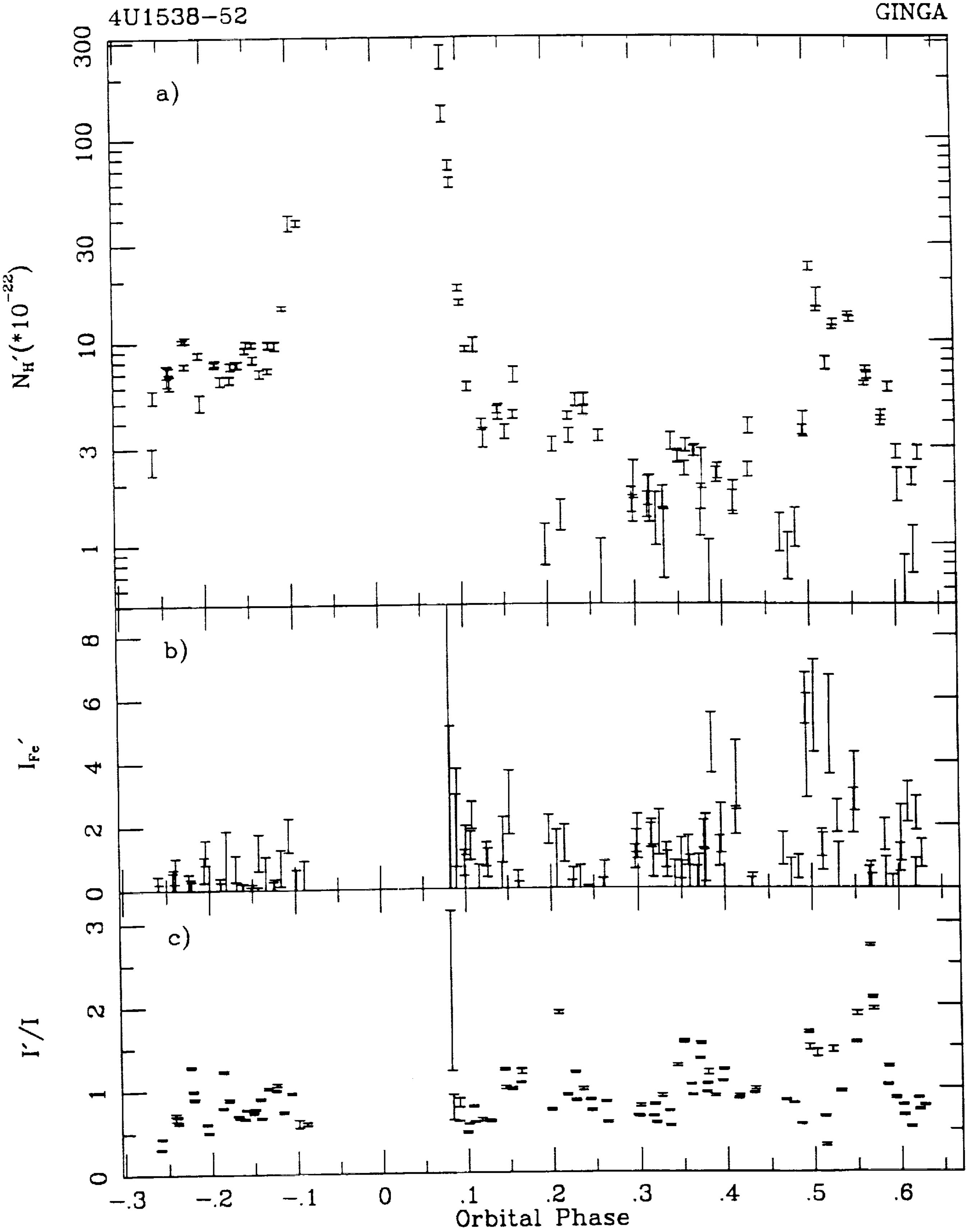
4U1538-52
GINGA
a)
b)
c)
N_H′(*10^-22)
300
100
30
10
3
1
I_Fe′
8
6
4
2
0
I′/I
3
2
1
0
-.3
-.2
-.1
0
.1
.2
.3
.4
.5
.6
Orbital Phase

Figure 2

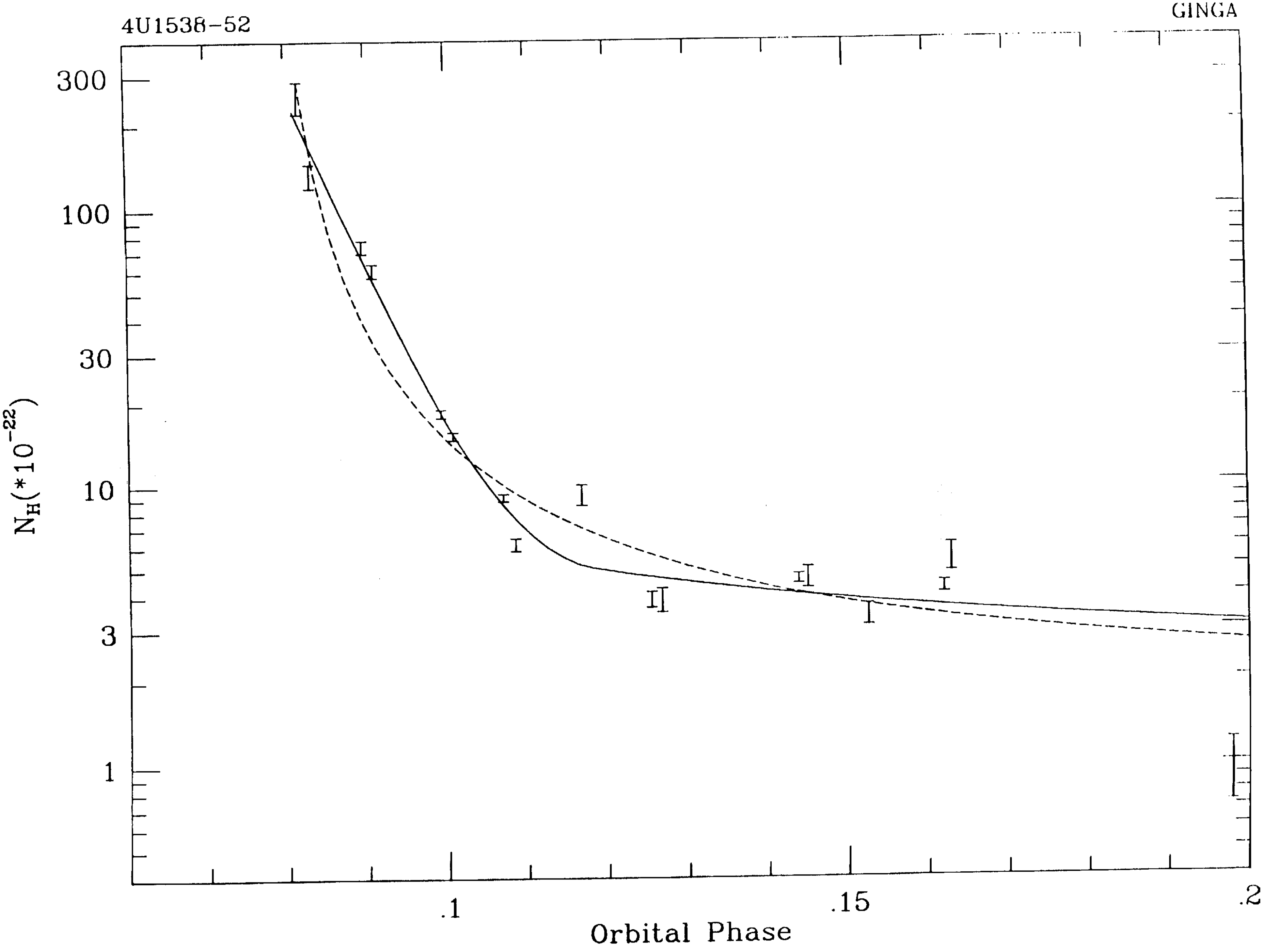

Figure 3

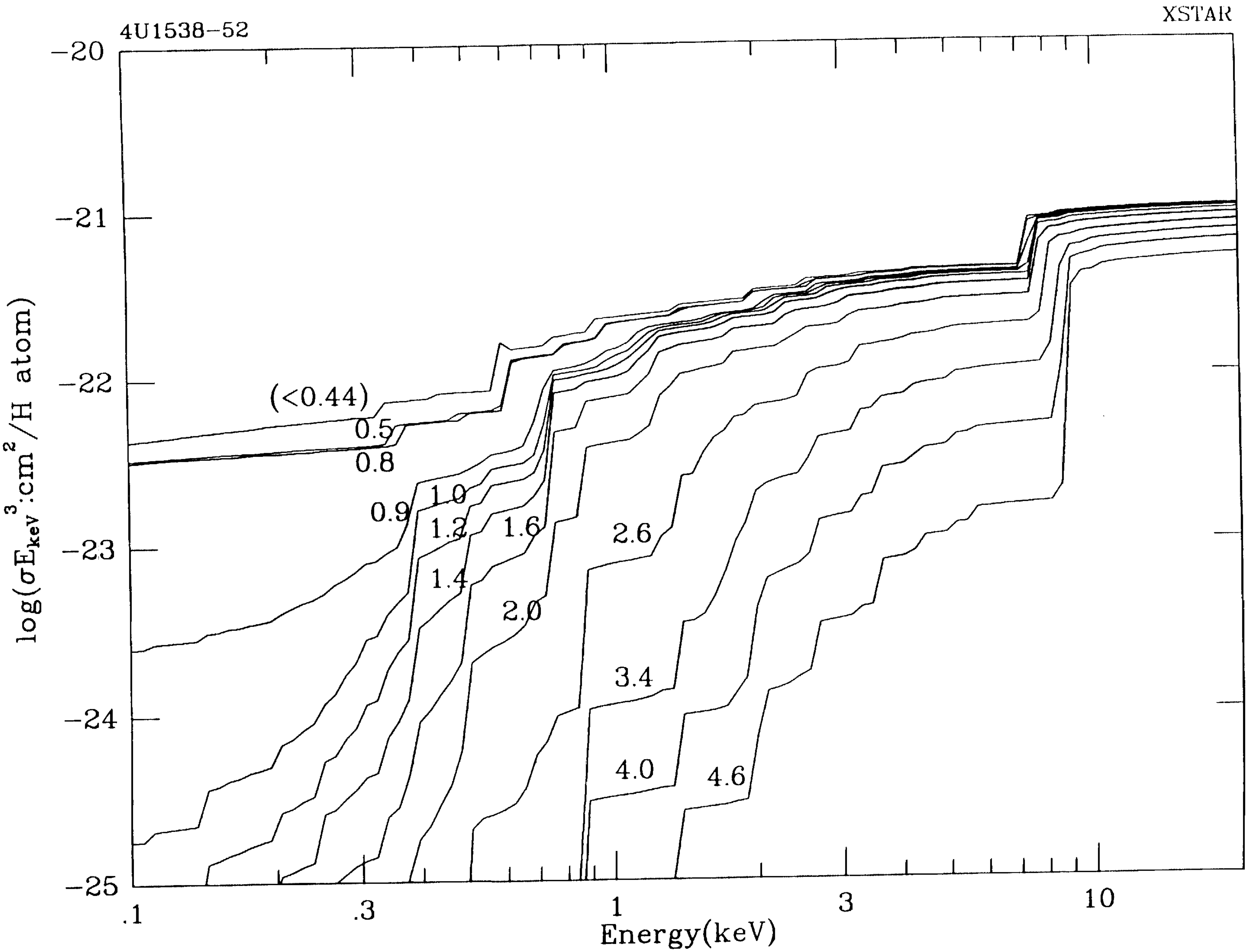
4U1538-52
XSTAR
-20
-21
-22
-23
-24
-25
log($\sigma E_{keV}{}^3$:cm^2/H atom)
.1
.3
1
3
10
Energy(keV)
(<0.44)
0.5
0.8
0.9
1.0
1.2
1.4
1.6
2.0
2.6
3.4
4.0
4.6

Figure 4

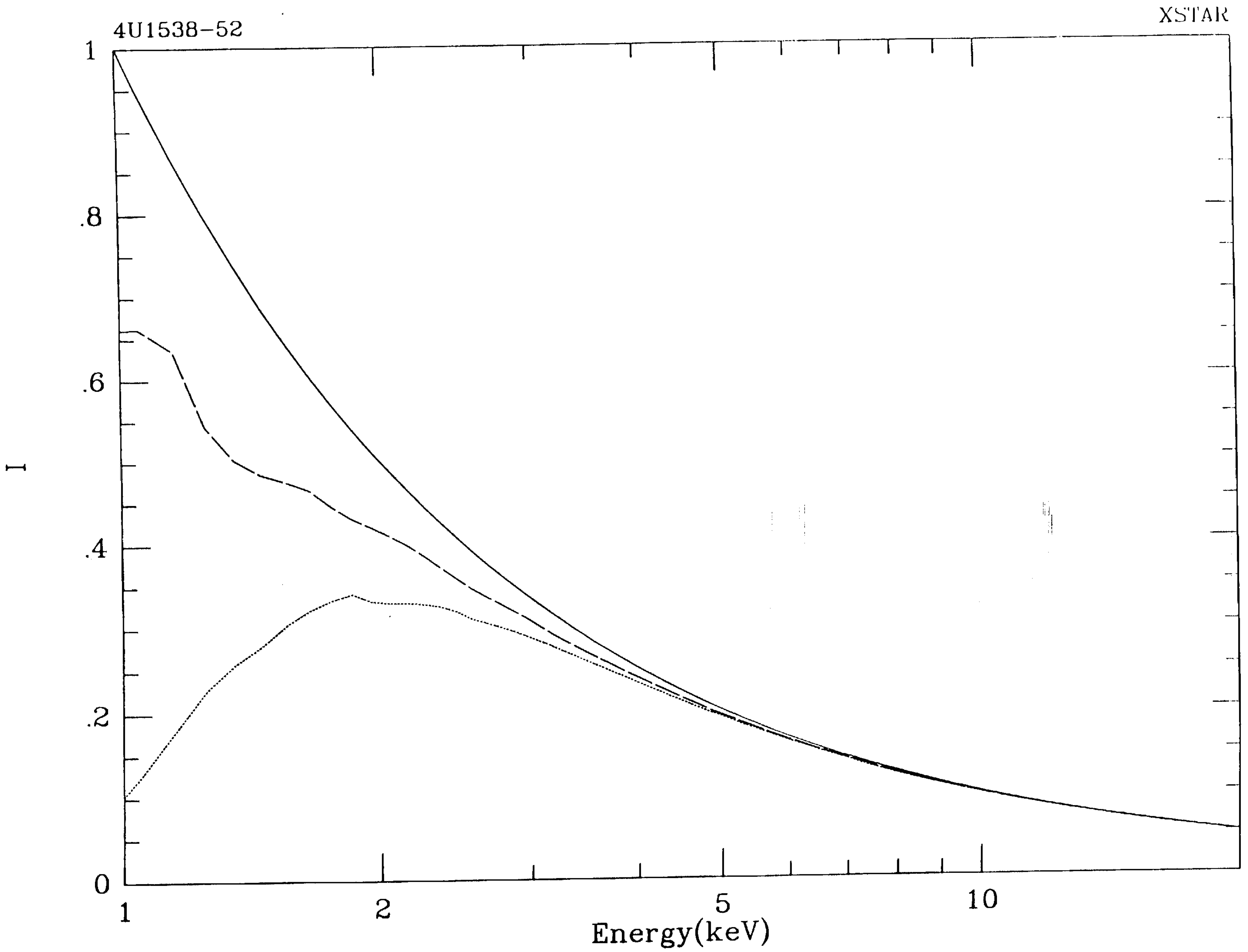

Figure 5

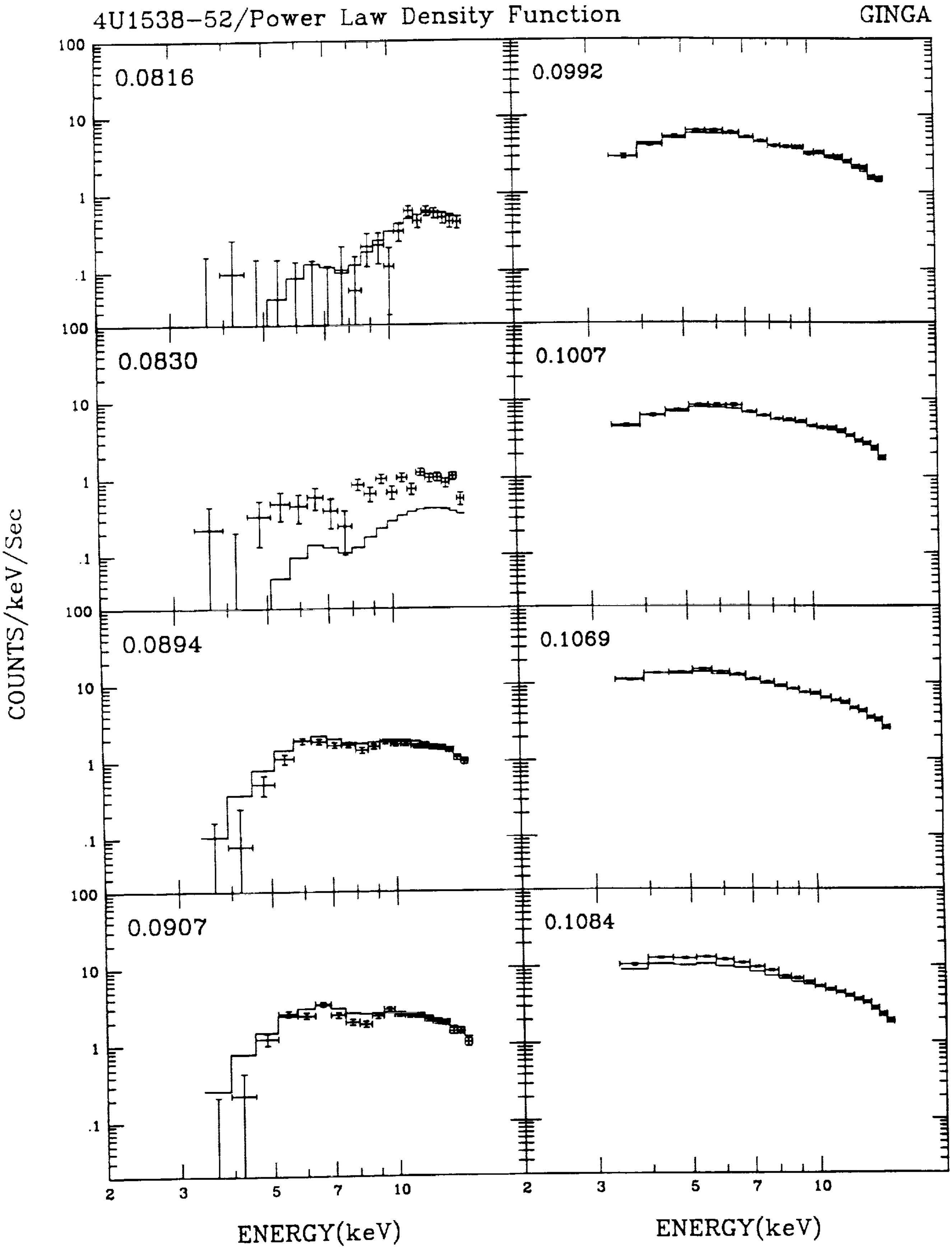
4U1538-52/Power Law Density Function
GINGA
0.0816
0.0830
0.0894
0.0907
0.0992
0.1007
0.1069
0.1084
100
10
1
.1
COUNTS/keV/Sec
2
3
5
7
10
ENERGY(keV)

Figure 6a

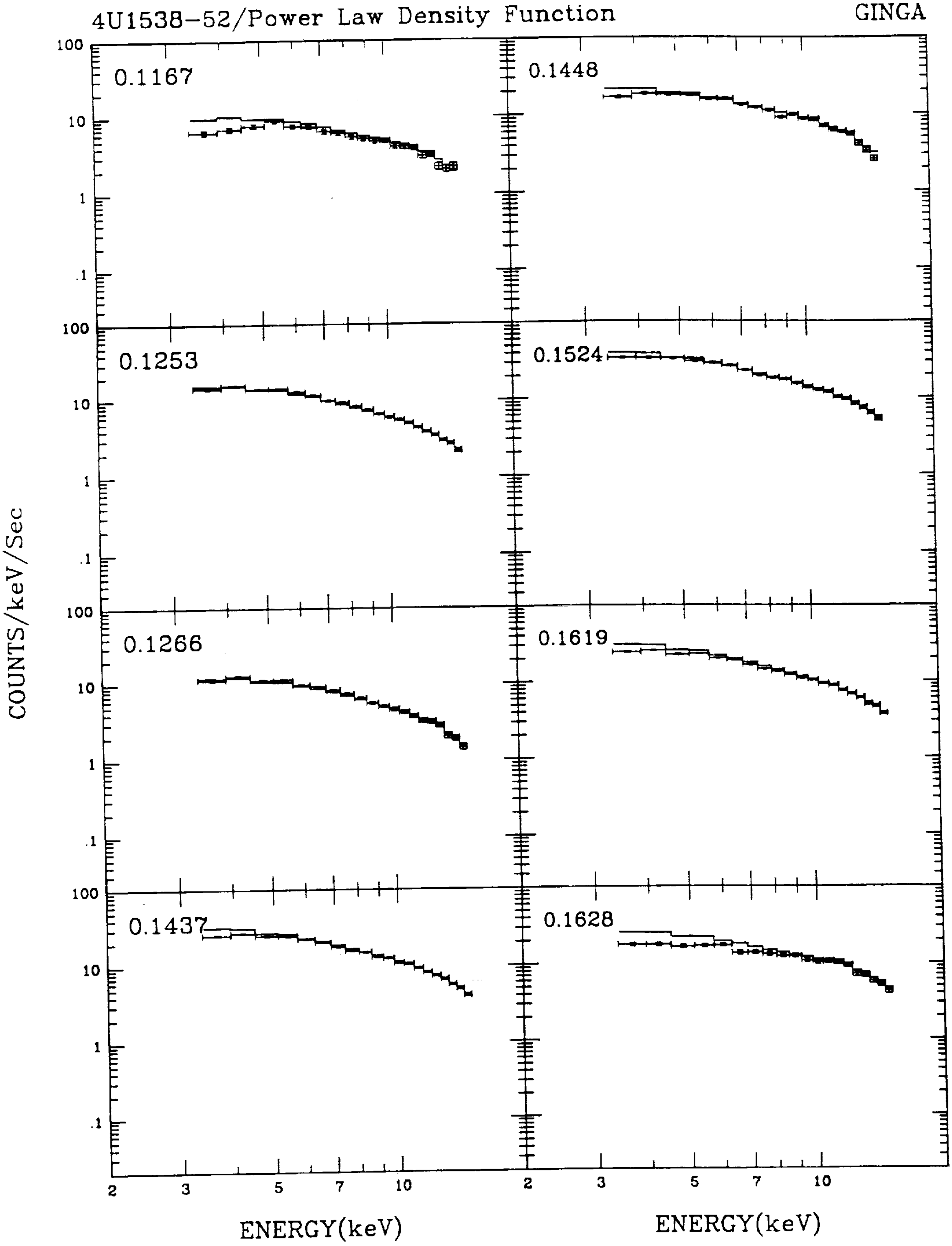

4U1538-52/Power Law Density Function
GINGA
0.1167
0.1448
0.1253
0.1524
0.1266
0.1619
0.1437
0.1628
100
10
1
.1
COUNTS/keV/Sec
2
3
5
7
10
ENERGY(keV)

Figure 6b

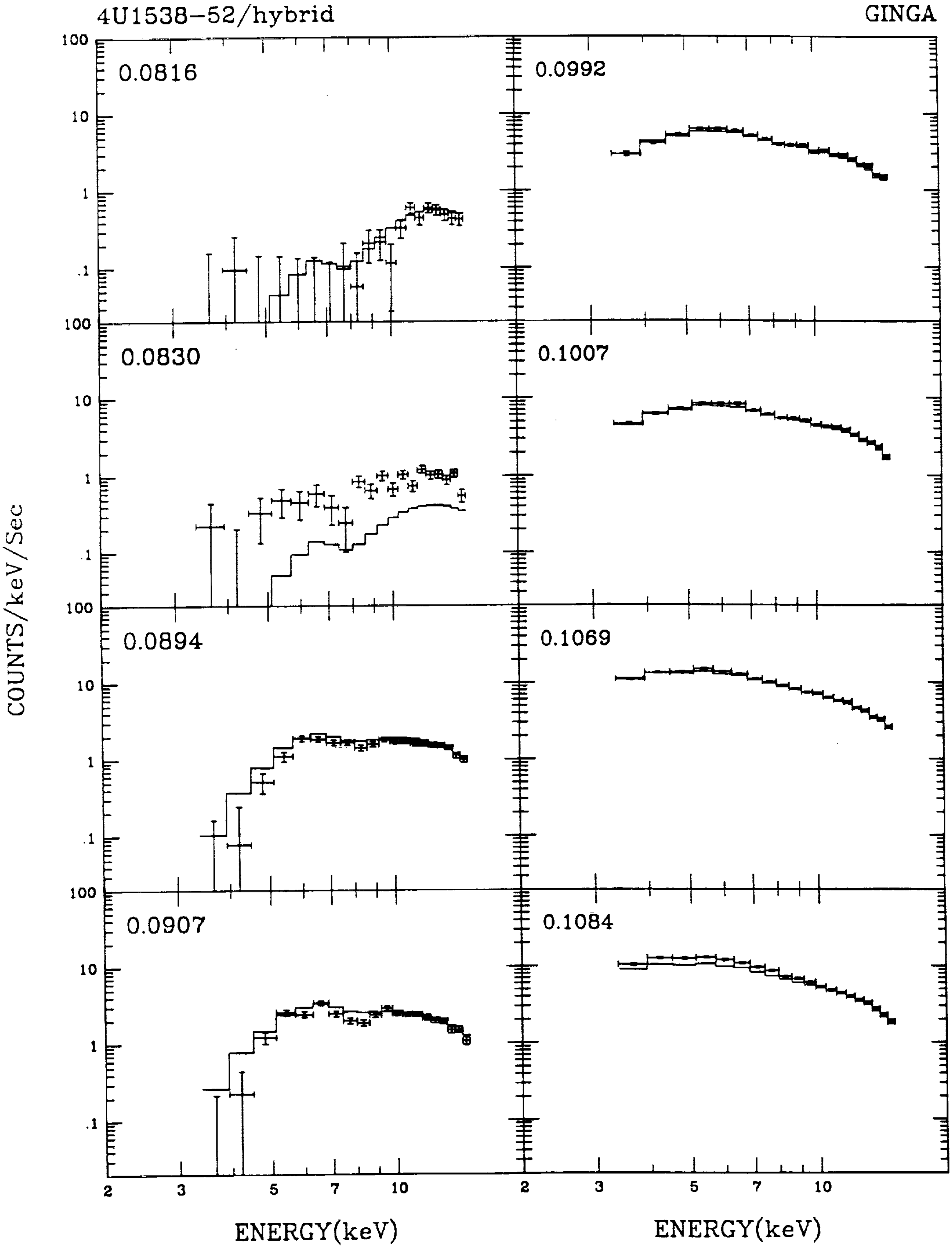
4U1538-52/hybrid
GINGA
COUNTS/keV/Sec
0.0816
0.0830
0.0894
0.0907
0.0992
0.1007
0.1069
0.1084
100
10
1
.1
2
3
5
7
10
ENERGY(keV)
ENERGY(keV)

Figure 7a

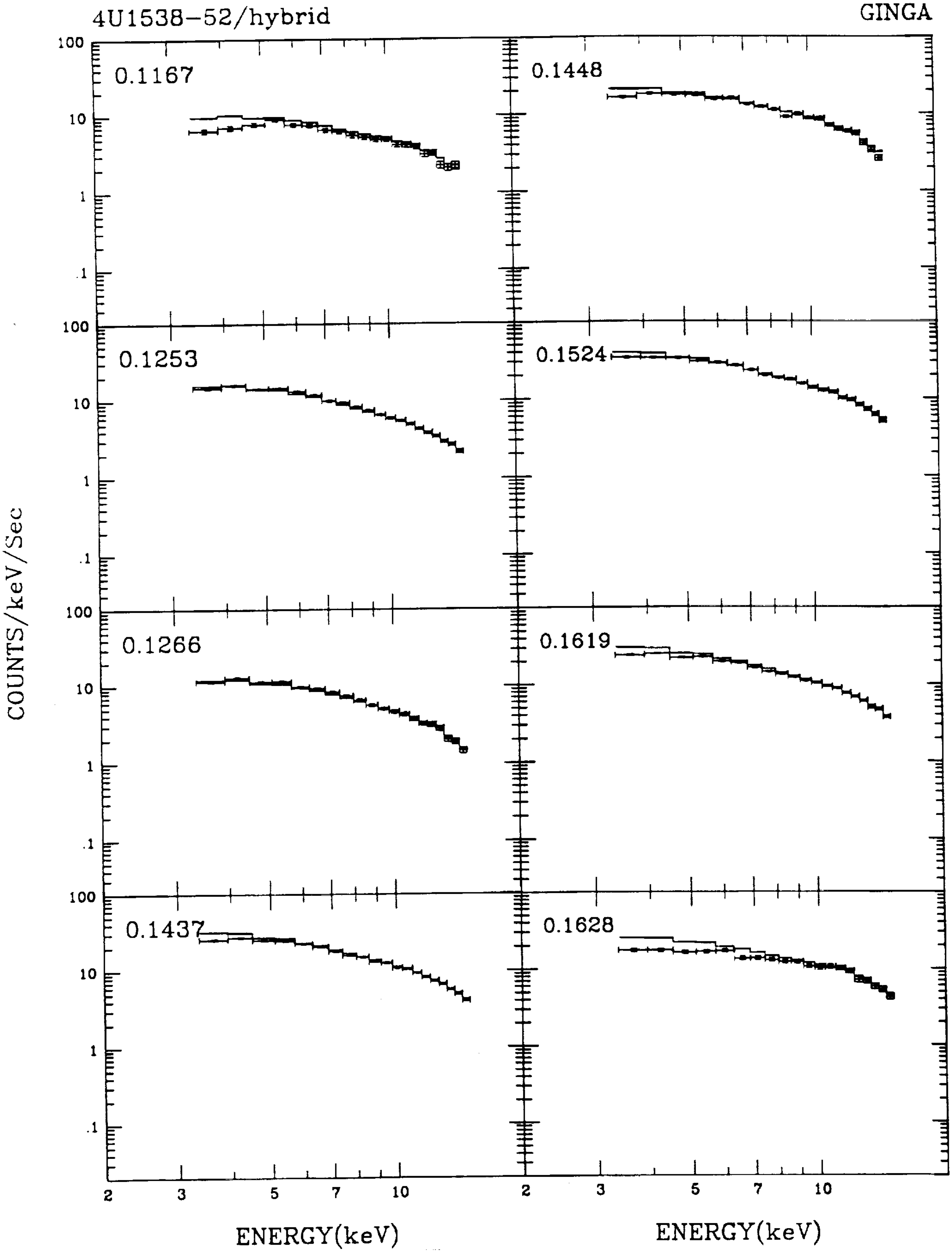
4U1538-52/hybrid
GINGA
0.1167
0.1448
0.1253
0.1524
0.1266
0.1619
0.1437
0.1628
100
10
1
.1
COUNTS/keV/Sec
2
3
5
7
10
ENERGY(keV)

Figure 7b

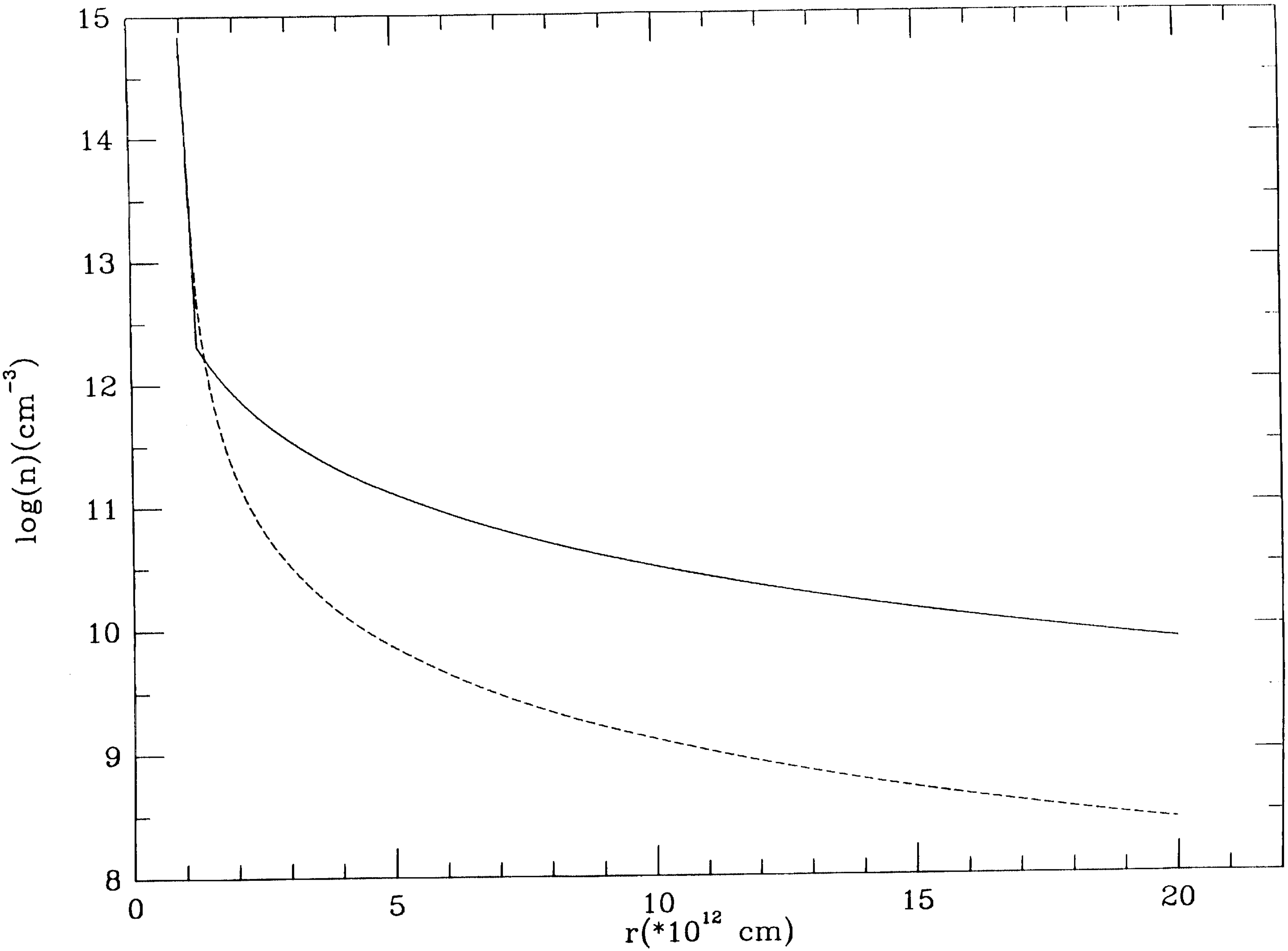

Figure 8

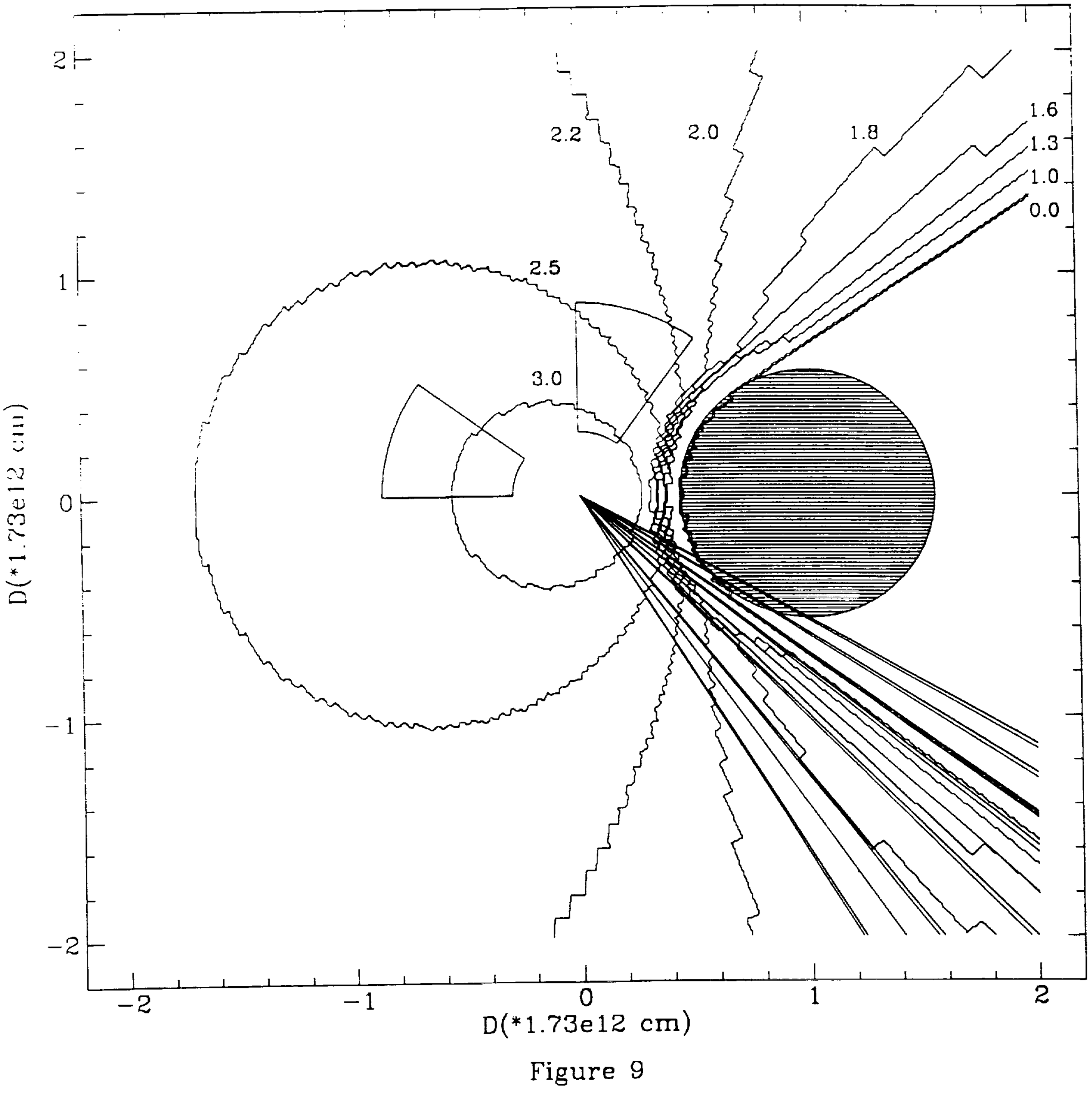

Figure 9

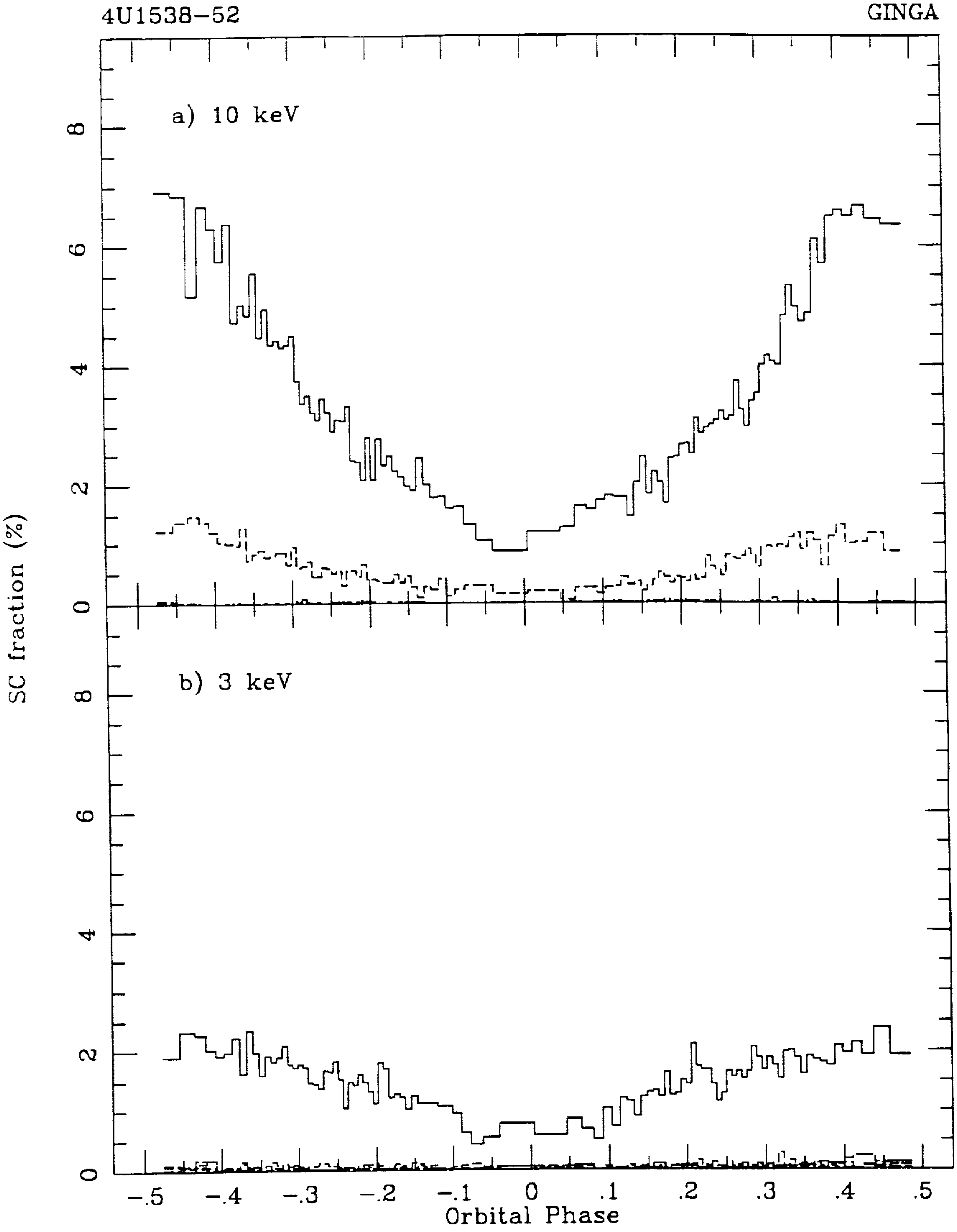
4U1538-52
GINGA
a) 10 keV
b) 3 keV
SC fraction (%)
0
2
4
6
8
-.5
-.4
-.3
-.2
-.1
0
.1
.2
.3
.4
.5
Orbital Phase

Figure 10

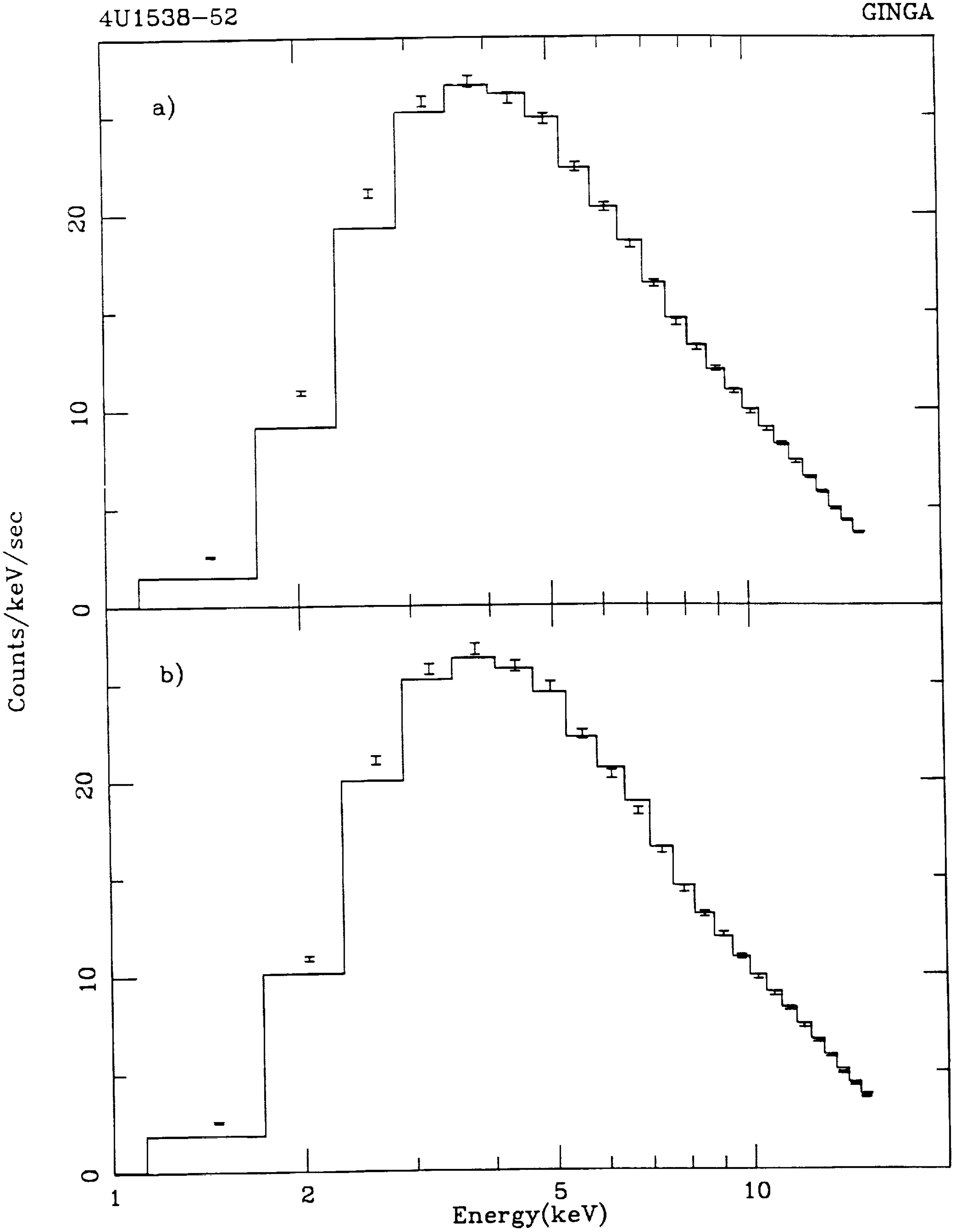
4U1538-52
GINGA
a)
b)
Counts/keV/sec
0
10
20
0
10
20
1
2
5
10
Energy(keV)

Figure 11

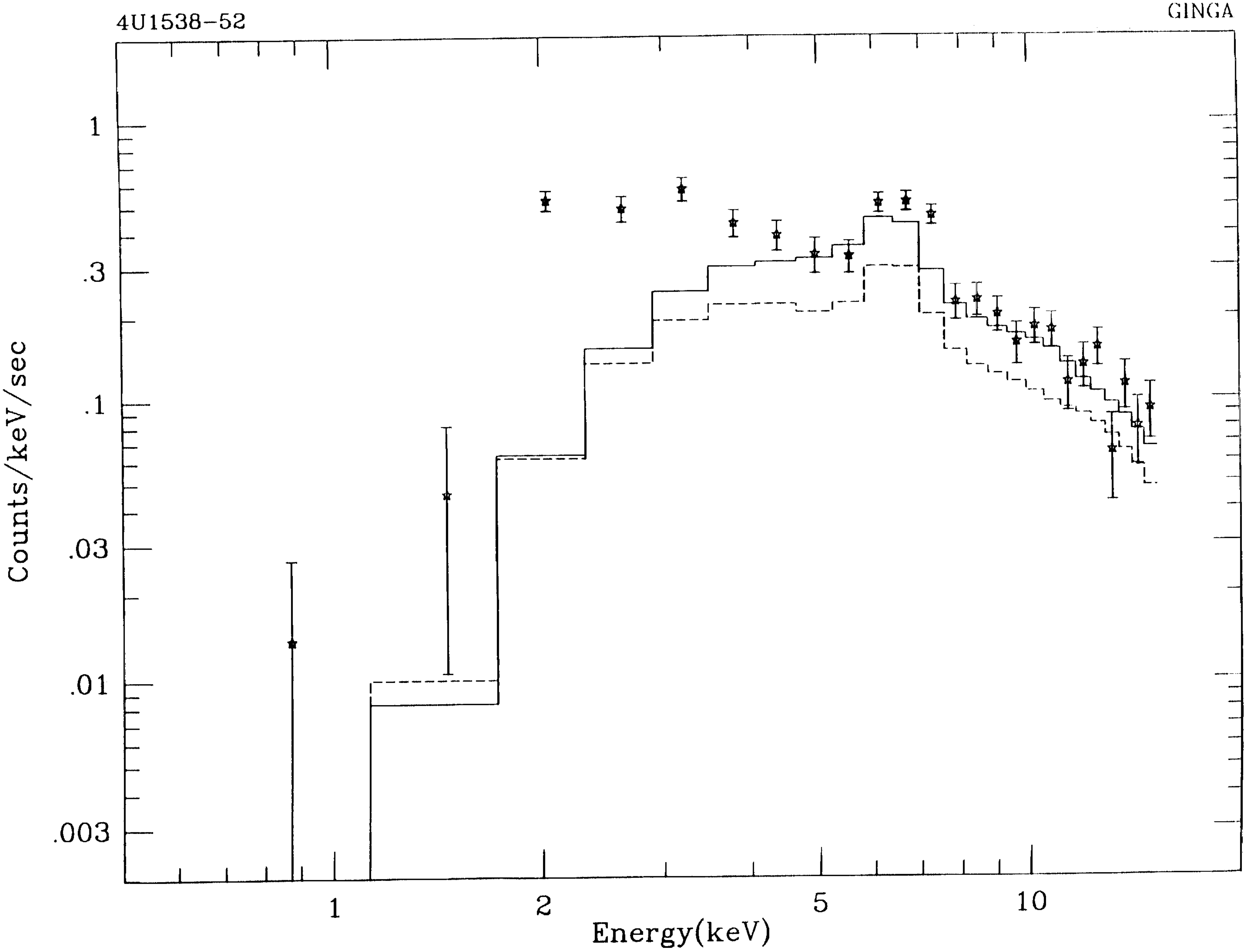

Figure 12

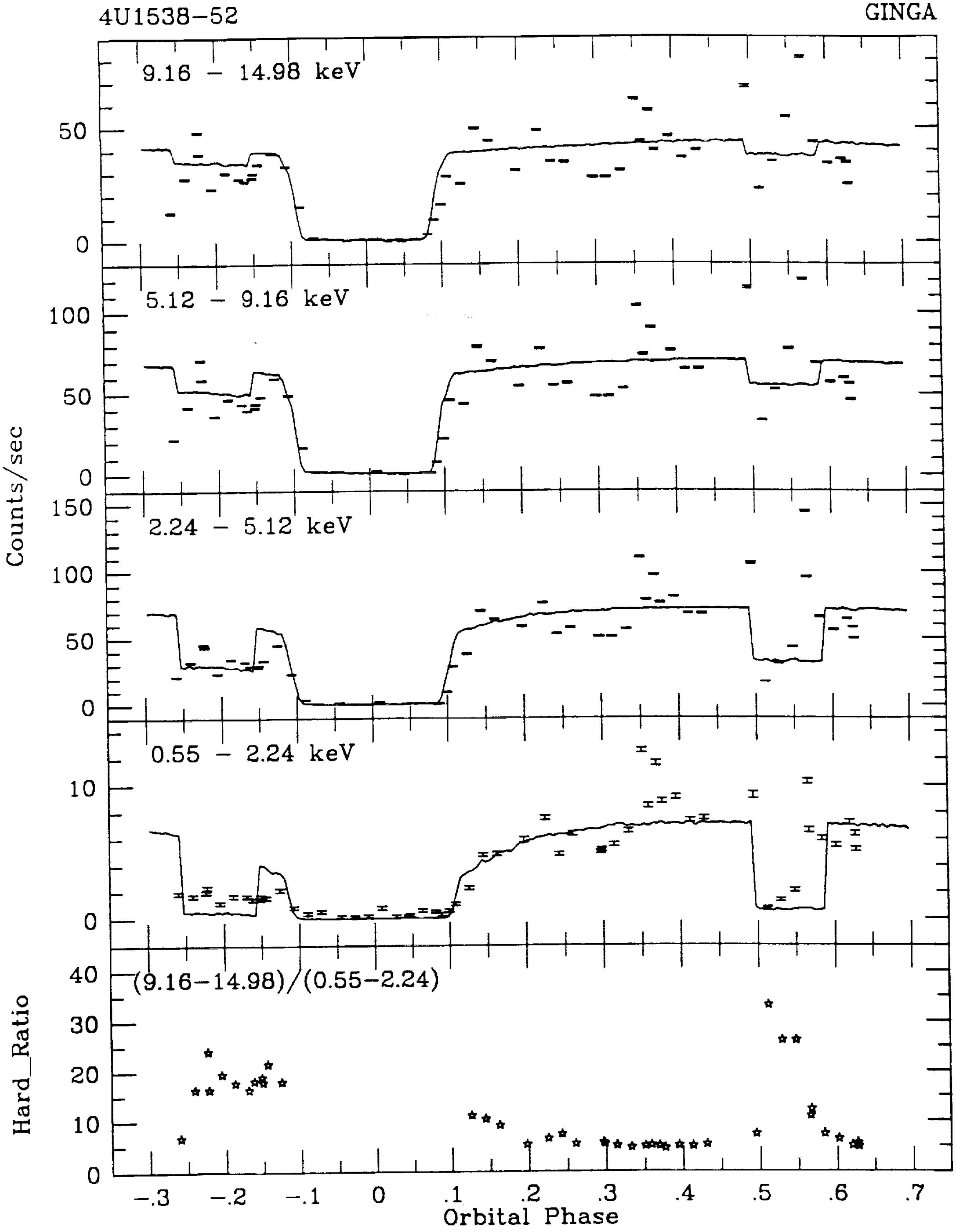

4U1538-52
GINGA
9.16 – 14.98 keV
5.12 – 9.16 keV
2.24 – 5.12 keV
0.55 – 2.24 keV
(9.16–14.98)/(0.55–2.24)
Counts/sec
Hard_Ratio
Orbital Phase
0
50
100
150
10
20
30
40
-.3
-.2
-.1
0
.1
.2
.3
.4
.5
.6
.7

Figure 13

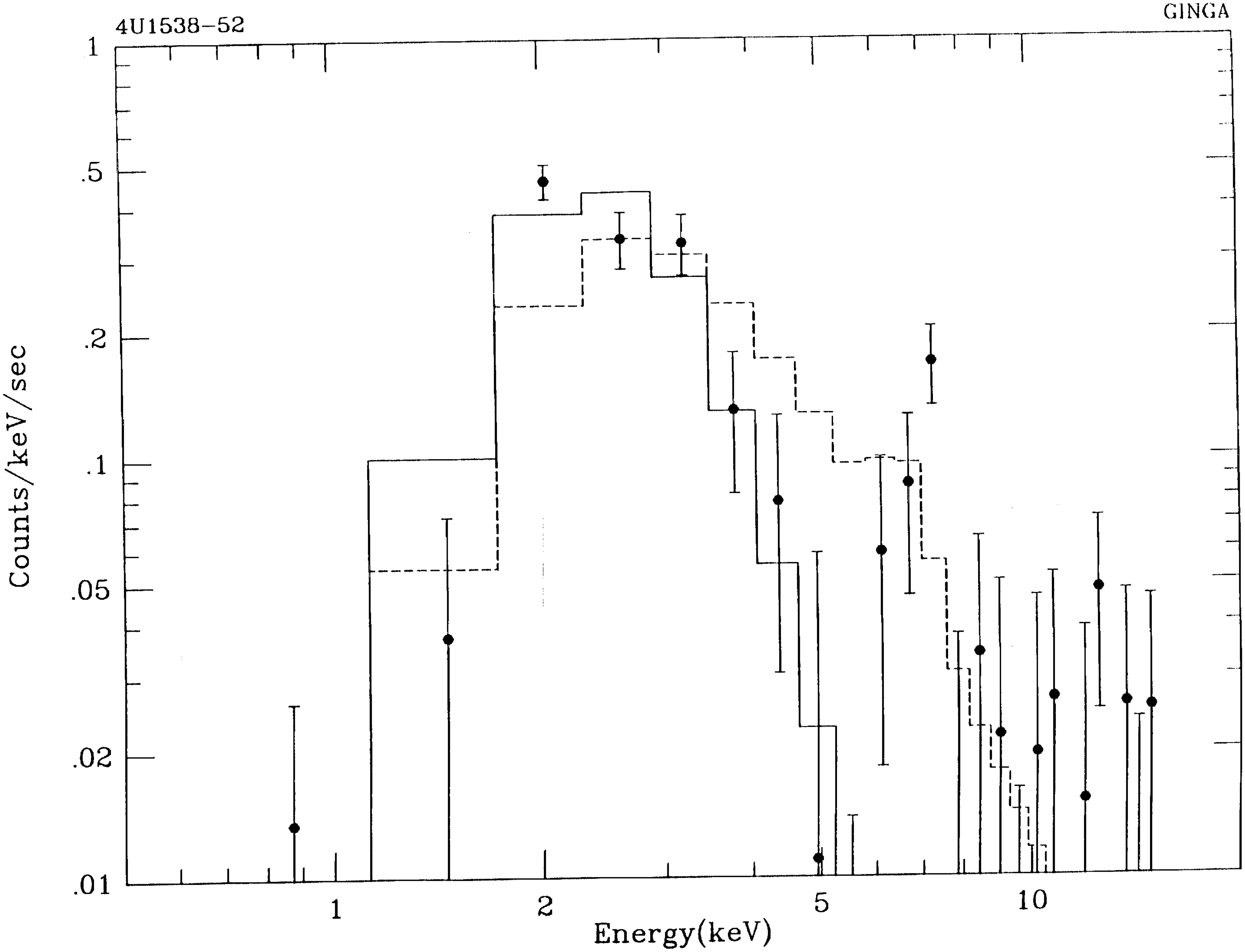

Figure 14

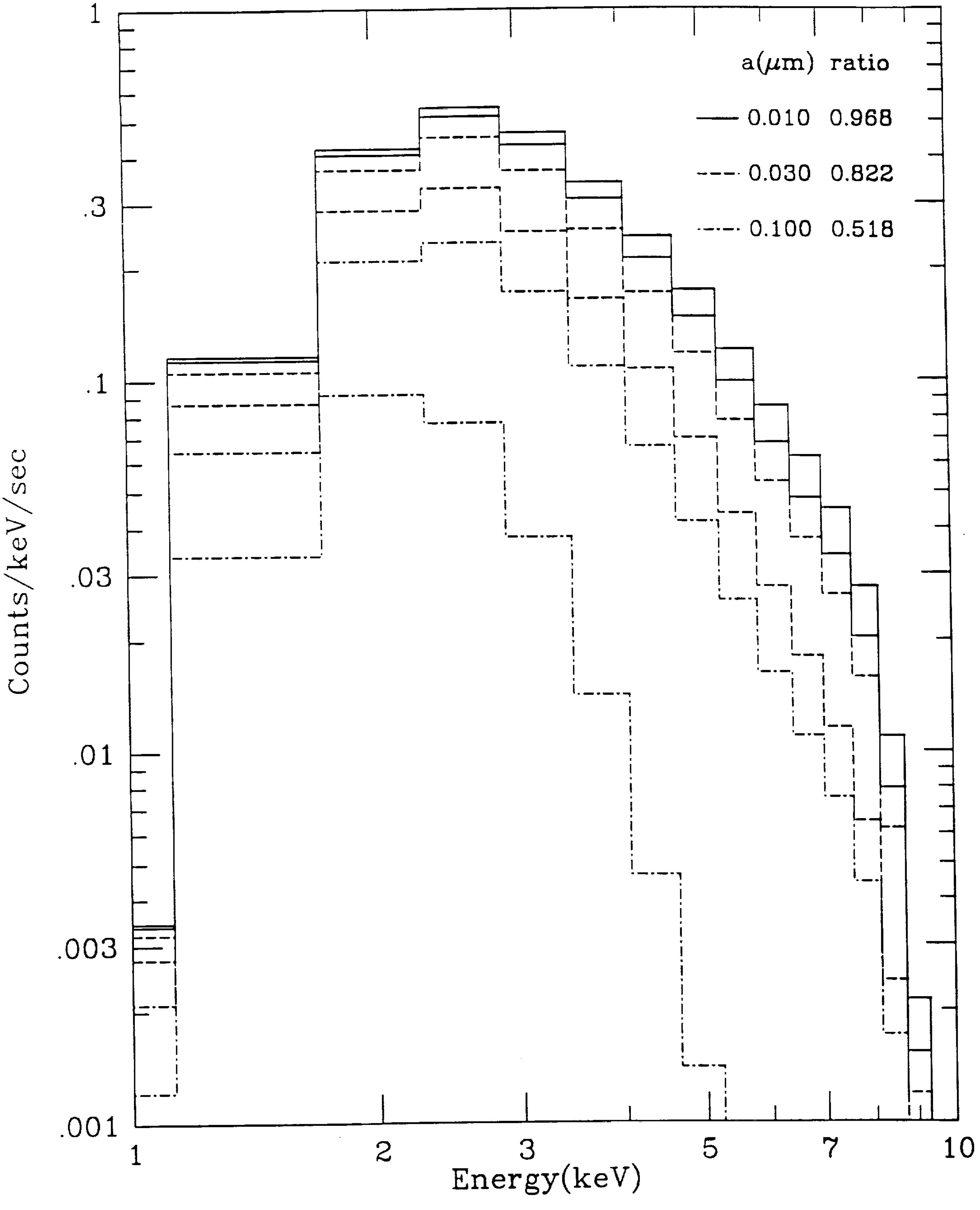

a(μm) ratio
0.010 0.968
0.030 0.822
0.100 0.518
Counts/keV/sec
1
.3
.1
.03
.01
.003
.001
1
2
3
5
7
10
Energy(keV)

Figure 15

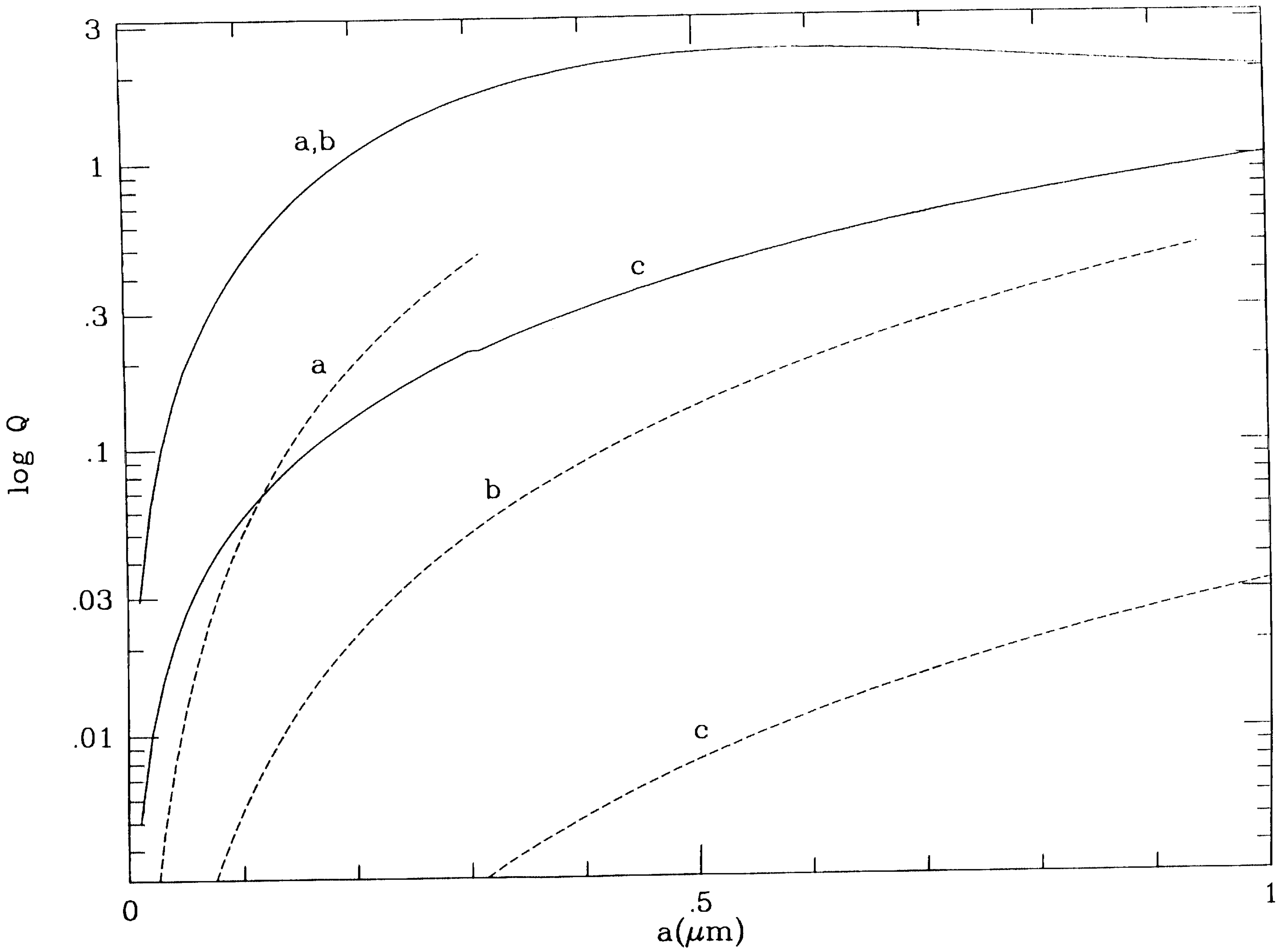

Figure 16

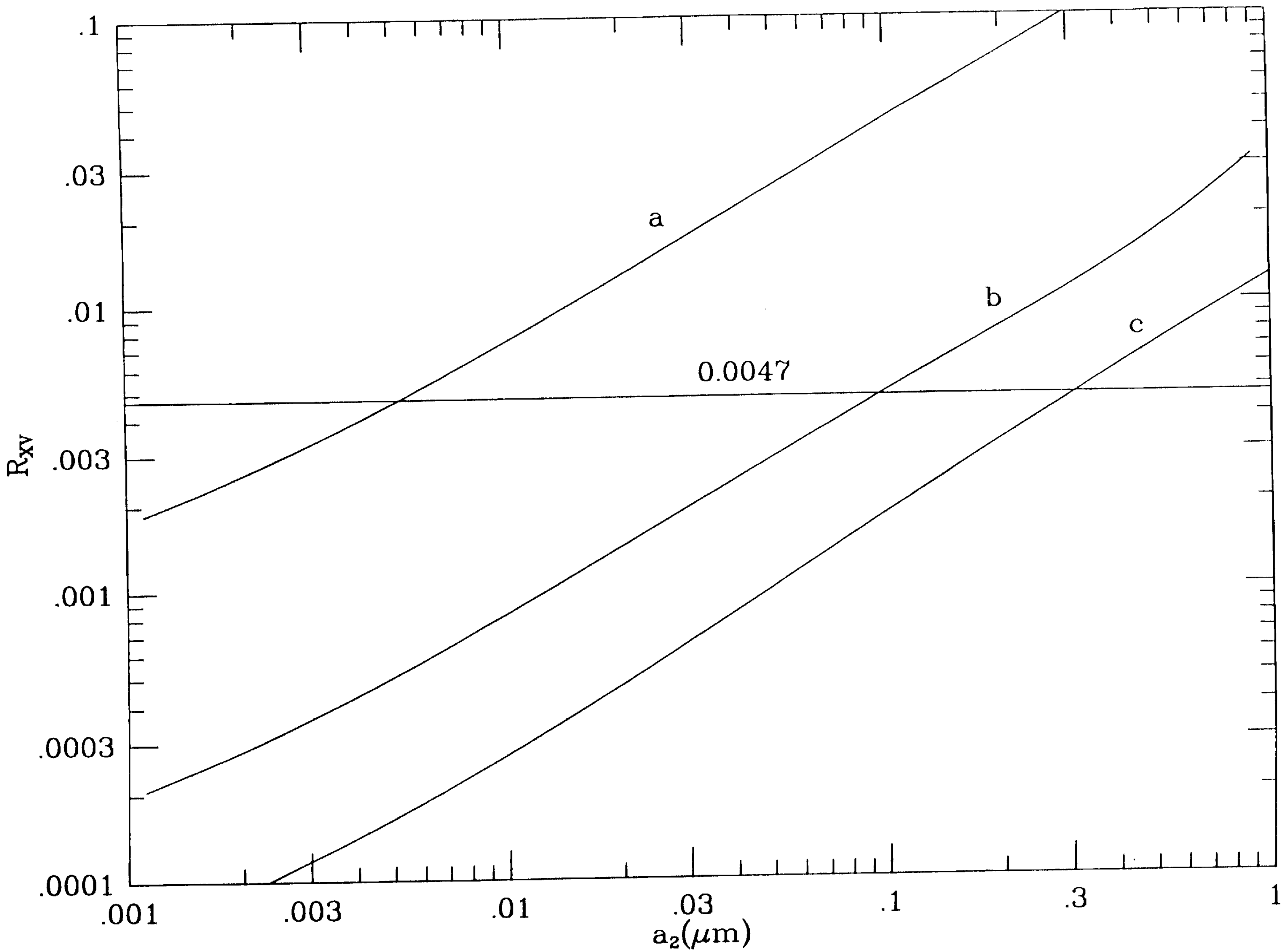

Figure 17

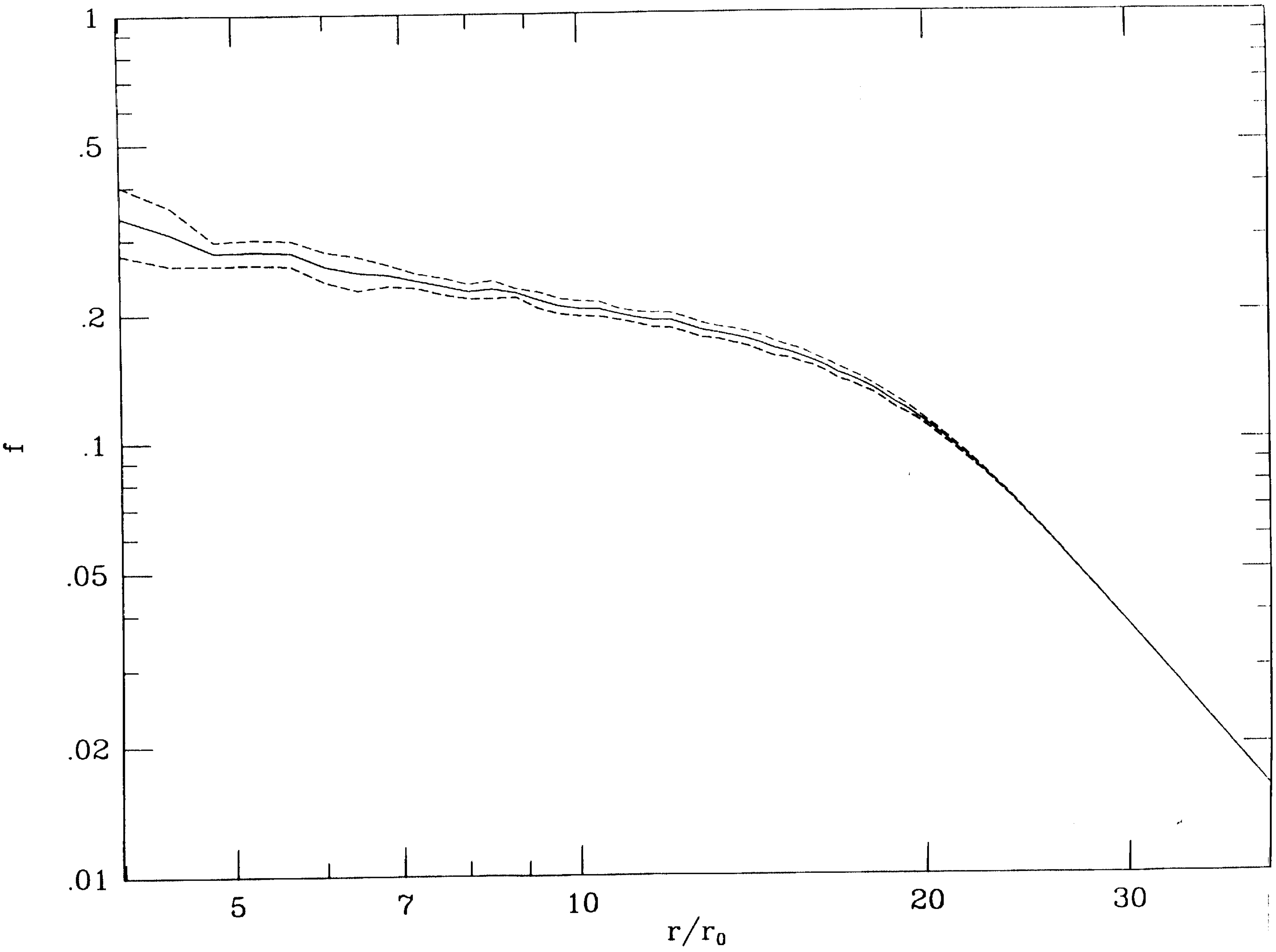

Figure 18